

# Holographic MIMO Communications with Arbitrary Surface Placements: Near-Field LoS Channel Model and Capacity Limit

Tierui Gong, *Member, IEEE*, Li Wei, Chongwen Huang, *Member, IEEE*, Zhijia Yang, Jiguang He, *Senior Member, IEEE*, Mérouane Debbah, *Fellow, IEEE*,  
and Chau Yuen, *Fellow, IEEE*

## Abstract

Envisioned as one of the most promising technologies, holographic multiple-input multiple-output (H-MIMO) recently attracts notable research interests for its great potential in expanding wireless possibilities and achieving fundamental wireless limits. Empowered by the nearly continuous, large and energy-efficient surfaces with powerful electromagnetic (EM) wave control capabilities, H-MIMO opens up the opportunity for signal processing in a more fundamental EM-domain, paving the way for realizing holographic imaging level communications in supporting the extremely high spectral efficiency and energy efficiency in future networks. In this article, we try to implement a generalized EM-domain near-field channel modeling and study its capacity limit of point-to-point H-MIMO systems that equips arbitrarily placed surfaces in a line-of-sight (LoS) environment. Two effective and computational-efficient channel models are established from their integral counterpart, where one is with a sophisticated formula but showcases more accurate, and another is concise with a slight precision sacrifice. Furthermore, we unveil the capacity limit using our channel model, and derive a tight upper bound based upon an elaborately built analytical framework. Our result reveals that the capacity limit grows logarithmically

Part of this article was accepted by ICC workshop 2023 [1]

T. Gong, and L. Wei are with the Engineering Product Development (EPD) Pillar, Singapore University of Technology and Design, Singapore 487372 (e-mails: tierui\_gong@sutd.edu.sg, wei\_li@mymail.sutd.edu.sg).

C. Huang is with the College of Information Science and Electronic Engineering, Zhejiang University, Hangzhou 310027, China (e-mails: chongwenhuang@zju.edu.cn).

Z. Yang is with Shenyang Institute of Automation, CAS, Shenyang 110016, China (e-mail: yang@sia.ac.cn).

J. He is with Technology Innovation Institute, Masdar City 9639, Abu Dhabi, United Arab Emirates (e-mail: jiguang.he@tii.ae).

M. Debbah is with the Technology Innovation Institute, Masdar City 9639, Abu Dhabi, United Arab Emirates, and also with the CentraleSupélec, University ParisSaclay, 91192 Gif-sur-Yvette, France (e-mail: merouane.debbah@tii.ae).

C. Yuen is with the School of Electrical and Electronics Engineering, Nanyang Technological University, Singapore 639798 (e-mails: chau.yuen@ntu.edu.sg).

with the product of transmit element area, receive element area, and the combined effects of  $1/d_{mn}^2$ ,  $1/d_{mn}^4$ , and  $1/d_{mn}^6$  over all transmit and receive antenna elements, where  $d_{mn}$  indicates the distance between each transmit and receive elements. Numerical evaluations validate the effectiveness of our channel models, and showcase the slight disparity between the upper bound and the exact capacity, which is beneficial for predicting practical system performance.

### Index Terms

Holographic MIMO, channel modeling, capacity limit, near-field LoS, arbitrary surface placement.

## I. INTRODUCTION

The sixth-generation (6G) wireless networks are envisioned to provide holographic communications with immersive experiences in supporting the extremely large amount of data traffic and a multitude of various upper-layer applications with a special requirement on high energy efficiency [2]. Massive multiple-input multiple-output (M-MIMO) technology was proposed as a critical enabler for the fifth-generation (5G) wireless networks, and its enhanced version, such as ultra-massive MIMO (UM-MIMO), was envisioned as a potential technology for 6G to meet the extreme requirement of data-rate. This is not sustainable in energy efficiency when the number of antennas scales up to be extremely large. The infeasibility is mainly caused by using the conventional power-hungry and cost-inefficient antenna technology and hardware structures, which requires a dedicated radio-frequency chain for each antenna element [3]. Even though this problem can be relieved to some extent by using hybrid analog-digital structures [4], [5], it is still not extendable for supporting future 6G with extremely large number of antenna elements, due to applications of the conventional antenna technology.

Holographic MIMO (H-MIMO) is recently envisioned to be a promising technology capable of revolutionizing the traditional M-MIMO and UM-MIMO, as well as facilitating the developments of various aspects of 6G [6]. H-MIMO exploits new antenna technologies, offering at least retained performance while reducing power consumption and cost. In particular, H-MIMO generally follows the holographic principle, where one or more reference waves, loaded by the feed ports, propagate successively to the antenna elements, thereby, generating the object waves via tunable elements [6], [7]. One of the typical realizations is using artificial meta-materials/metasurfaces, allowing electromagnetic (EM) wave manipulations with low-cost, low

power consumption, and various expected EM responses. In general, one of the prominent features of H-MIMO is that the antenna aperture, known as the antenna surface, appears to be almost continuous with nearly countless number of elements packed over it. In addition, another conspicuous characteristic of H-MIMO is its electronically large surface area, which is used for combating large path-loss in high frequencies, and is made feasible owing to the low-cost and low power consumption nature. These new features, not found in conventional M-MIMO systems, bring new challenges and opportunities for H-MIMO communications.

Since the the nearly continuous surface, and the inherently powerful capability in EM wave control, H-MIMO can record almost completed wave information in space, and manipulate EM waves in almost arbitrary degree of freedom, which can promisingly approach the fundamental limit of the wireless environment [8]. Furthermore, the significantly less than half-a-wavelength spacing between elements inevitably causes strong mutual couplings among antenna elements, which is envisioned to be exploited for achieving the super-directivity [9]. To unveil the fundamental limit and study the mutual coupling effect, one of the critical challenges is to properly model the H-MIMO system from a more fundamental EM perspective. In addition, the electrically large surface of H-MIMO shifts communication regions from the far-field to the near-field. Different from far-field communications, prevalent in conventional M-MIMO systems by merely exploiting the angle information, the near-field communications induced by H-MIMO leverage both angle and distance information in assisting transmissions. Consequently, H-MIMO systems will significantly enlarge the degree-of-freedom in communications. In this regard, H-MIMO paves the way for holographic imaging level near-field communications [6]. Generally speaking, both EM-domain modeling and analysis, especially for near-field cases, are critical to H-MIMO, where the EM-domain channel modeling and capacity limit analysis are of great significance.

#### *A. Prior Studies*

In channel modeling, new features of H-MIMO inevitably introduce fundamental changes that are critical to unveil the system performance and perform system designs. Conventional channel models, such as the classic Rayleigh fading channel model [10] and its correlated version [11], as well as the cluster-based channel model [12], [13], are generally built for far-field scenarios and are all based upon mathematical abstractions, depicting the wireless channel via mathematical representations, while ignoring physical phenomena of the EM wave propagation. This is, however, insufficient to describe the wireless channel for H-MIMO communications.

As shown recently in [14]–[16], the authors proposed to describe the wireless channel based on an EM principle, where they studied the small-scale fading for the far-field scenarios. As antenna surfaces tending large, the near-field line-of-sight (LoS) channel should be considered. In most recent studies [17], [18], the near-field LoS channel is described using a spherical wave propagation model, which is more believed as a mathematical abstraction without putting more emphasis on EM propagation phenomena. Recent work [19] proposed an EM-compliant near-field LoS channel model for H-MIMO, which only considers the parallel placement of surfaces. This leads to the failure in capturing channel responses for arbitrary surface placements, which is the general case in practical deployments. This restricts its applications in practical scenarios.

In capacity limit analysis, most prior studies are based upon the mathematically abstracted channel model and assume a parallel placement of antenna surfaces. The works [20]–[22] considered the large intelligent surfaces or extremely large MIMO aided multiple single-antenna user system, and studied the system performance under near-field LoS channel using the spherical wave propagation channel model. These works analyze based on mathematical abstractions not only in channel modeling but also in system modeling [21], [22]. In addition, a few studies perform their analyses with the EM-domain modeling incorporated. Specifically, [16], considering the far-field small-scale fading in a multi-user H-MIMO system, analyzed the capacities of different transmission schemes by using an established EM-domain channel model. This model is a multi-user extension of [14], [15]. A comprehensive study based upon a rigorous EM derivation can be found earlier in [23]. Another recent work [24], starting from an EM-domain system modeling on continuous surfaces, while using a simple spherical wave propagation channel model, analyzed the performance of a point-to-point H-MIMO system in near-field LoS environment. Moreover, [25] established an EM-domain system model for a point-to-point H-MIMO system in the near-field LoS channel, where the power gain and degree-of-freedom were analyzed and several useful results were provided for certain special cases. Some of the foundations can be dated back to [26], [27], built for optical systems. These EM-domain driven studies mainly focus on H-MIMO systems with a specific surface placement, i.e., the transmit and receive surfaces are located in a parallel setup, which has a limited generalization to practical scenarios with arbitrary surface placements. Moreover, we emphasize that the studies based on EM-domain modeling, such as [23], [25], incorporate multiple integral operations in their models, failing to provide tractable models for system designs and signal processing in spite of the applicability to unveil the fundamental limits.

In summary, the prior studies mostly focus on using mathematical abstractions for channel modeling and ignoring the true wave propagation phenomena, especially for the near-field LoS channel modeling, based on which the capacity limit or other performance metrics are analyzed. Hopefully, a few recent studies analyzed the system in an EM-domain, however, they mainly considered certain special scenarios with limited practical applications.

### *B. Contributions*

To mitigate the gaps, we focus on a point-to-point H-MIMO system with arbitrary surface placements, and propose to depict the whole system from an EM perspective. More importantly, we establish the generalized EM-domain near-field LoS channel models and unveil the capacity limit on this basis. The details of our contributions are listed as follows.

- We present an effective representation approach for characterizing the arbitrariness of surface placements, capable of controlling the location and orientation of any surface (and its elements) as well as two different surface (element) shapes. This approach also allows us to represent arbitrary point on the surface by two defined unit vectors, and to denote the  $z$ -axis component of a surface point by its  $x$ -axis and  $y$ -axis components, facilitating the subsequent near-field LoS channel modeling.
- We study a generalized EM-domain channel modeling for near-field LoS scenarios, by employing our representation approach for surface placements, and utilizing the Taylor series expansion to tackle the implicit form and computationally-infeasible problem caused by multiple integrals. Accordingly, a sophisticated but more accurate coordinate-dependent channel model (CD-CM), depending on the absolute location of antenna elements, is first established. With moderate approximations, the CD-CM is further simplified to a concise coordinate-independent channel model (CI-CM) with a slight precision sacrifice, which is merely determined by the relative distances and their directions.
- We further examine the capacity limit of H-MIMO systems using the established CI-CM in a rigorous deviation. The analysis is performed based upon an analytical framework, incorporating formally defined transmit and receive patterns and a resulting convenient channel decomposition. These patterns indicate a series of orthogonal bases, capable of depicting any current distribution, electric field and the tensor Green's function based wireless channel. This framework facilitates our analysis in deriving a tight closed-form capacity upper bound. It reveals that the capacity grows logarithmically with the product

of transmit element area, receive element area, and combined effects of  $1/d_{mn}^2$ ,  $1/d_{mn}^4$ , and  $1/d_{mn}^6$  over all transmit and receive antenna elements, where  $d_{mn}$  is the distance between each transmit and receive elements.

- We finally evaluate the established channel models and capacity limit through extensive numerical simulations. The results validate the feasibility of our channel models and demonstrate the H-MIMO capacity limit, offering various insights for system designs.

### C. Organizations

The rest of this article is organized as follows: In Section II, we establish an EM-domain system model and provide an effective representation approach for surface placements. Later in Section III, near-field LoS channel models are established. We further present an analytical framework and perform analysis on the capacity limit in Section IV. Extensive numerical results are provided in Section V, and conclusions are made in Section VI.

## II. H-MIMO SYSTEM MODEL AND SETUP

In the following of this section, we focus on providing the EM-domain system model and characterizing the arbitrariness of surface placements. Particularly, we consider an H-MIMO communication system consisting of one transmitter (TX) communicating with a receiver (RX). Both TX and RX are equipped with almost countless infinitesimal antenna elements, forming almost continuous antenna surfaces. For convenience, we denote by  $N = N_h \times N_v$  the overall number of antenna elements of TX, consisting of  $N_h$  and  $N_v$  antenna elements in the horizontal direction and the vertical direction, respectively. Likewise, the RX has an overall  $M = M_h \times M_v$  antenna elements. Besides, we assume that the antenna elements are uniformly distributed over the surface, and each TX element has an area of  $s_T$  with a horizontal length  $l_T^h$  and a vertical length  $l_T^v$ . Accordingly, the overall surface area of TX can thus be derived as  $A_T = N s_T$ . This is extended in a similar way to the RX with element area  $s_R$ , horizontal length  $l_R^h$ , vertical length  $l_R^v$ , and an overall surface area  $A_R = M s_R$ . Moreover, we depict the whole system in Cartesian coordinates, and consider an arbitrary placement of antenna surfaces, which is more generalized than those commonly considered parallel placement [16], [19], [20], [24], [25].

### A. EM-domain System Model

As previously described, H-MIMO is capable of controlling the EM waves in an unprecedented flexibility, whose communication model needs to be depicted from the EM perspective. In

general, one can employ the current distribution and the electric field pair for demonstrating the transmit and receive relation. Specifically, the electric field  $\mathbf{e}(\mathbf{r}) \in \mathbb{C}^{3 \times 1}$  measured at a certain point location  $\mathbf{r}$  is an instance excited by the current distribution  $\mathbf{j}(\mathbf{t}) \in \mathbb{C}^{3 \times 1}$  imposed at a different point location  $\mathbf{t}$  after passing through the wireless channel  $\mathbf{H}_{\mathbf{r}\mathbf{t}} \in \mathbb{C}^{3 \times 3}$ . Since the whole system is located in the three-dimensional space, the current distribution and the electric field, oriented in arbitrary directions, can be represented by three sub-components as  $\mathbf{j}(\mathbf{t}) = [j^x, j^y, j^z]^T$  and  $\mathbf{e}(\mathbf{r}) = [e^x, e^y, e^z]^T$ , respectively, corresponding to  $xyz$ -axis. Their connecting wireless channels  $[\mathbf{H}_{\mathbf{r}\mathbf{t}}]_{pq} = H_{pq}$ ,  $p, q \in \{x, y, z\}$  map current distribution sub-components to electric field sub-components from the  $q$ -orientation to the  $p$ -orientation.

To demonstrate this, we focus on a current distribution  $\mathbf{j}(\mathbf{r}_n)$ , imposed at location  $\mathbf{t}_n = [x_n, y_n, z_n]^T$  of the TX surface. Due to the imposed current distribution, the incurred radiated electric field, measured at an arbitrary location  $\mathbf{r}_m = [x_m, y_m, z_m]^T$  within the region of the  $m$ -th antenna element of RX surface, is given by [28]

$$\mathbf{e}(\mathbf{r}_m) = \frac{\eta}{2\lambda} \int_{s_T} \mathbf{G}(\mathbf{r}_m, \mathbf{t}_n) \mathbf{j}(\mathbf{t}_n) d\mathbf{t}_n + \mathbf{w}(\mathbf{r}_m), \quad (1)$$

where  $\eta$  is the intrinsic impedance of free-space (i.e.,  $376.73 \Omega$ ), and  $\lambda$  is the free-space wavelength;  $\mathbf{w}(\mathbf{r}_m)$  indicates the noise measured at  $\mathbf{r}_m$ , following  $\mathcal{CN}(0, \sigma_w^2)$ ;  $\mathbf{G}(\mathbf{r}_m, \mathbf{t}_n) \in \mathbb{C}^{3 \times 3}$  is the tensor Green's function, given by

$$\mathbf{G}(\mathbf{r}_m, \mathbf{t}_n) = \frac{-i}{4\pi d_{mn}} \left( \mathbf{I}_3 + \frac{1}{k_0^2} \nabla \nabla^T \right) e^{ik_0 d_{mn}}, \quad (2)$$

where  $i^2 = -1$ ,  $\mathbf{I}_3$  is the  $3 \times 3$  identity matrix;  $k_0$  denotes the free-space wavenumber,  $k_0 = \frac{2\pi}{\lambda}$ ;  $\nabla = [\frac{\partial}{\partial x}, \frac{\partial}{\partial y}, \frac{\partial}{\partial z}]^T$  represents the gradient operator;  $d_{mn} \triangleq \|\mathbf{d}_{mn}\|_2 \triangleq \|\mathbf{r}_m - \mathbf{t}_n\|_2$  with  $\|\cdot\|_2$  denoting the  $l_2$  norm of a vector. On this basis, the overall electric field of each receive antenna element can be obtained as a sum of  $\mathbf{e}(\mathbf{r}_m)$  over the surface area  $s_R$ , i.e.,

$$\mathbf{e}_m = \int_{s_R} \mathbf{e}(\mathbf{r}_m) d\mathbf{r}_m = \frac{\eta}{2\lambda} \int_{s_R} \int_{s_T} \mathbf{G}(\mathbf{r}_m, \mathbf{t}_n) \mathbf{j}(\mathbf{t}_n) d\mathbf{t}_n d\mathbf{r}_m + s_R \mathbf{w}_m, \quad (3)$$

where we use the assumption that the noise is uniformly distributed over the whole  $s_R$  area, namely,  $\mathbf{w}(\mathbf{r}_m) \triangleq \mathbf{w}_m$ . We emphasize that (3) builds the input-output model of each  $mn$ -pair, which can depict any non-uniform current distributions. However, it is too complicated to integrate this model for depicting the whole H-MIMO system. To further simplify this model, it is reasonable to assume that the current distribution imposed to the antenna element is uniformly distributed over each area  $s_T$ . namely,  $\mathbf{j}(\mathbf{r}_n) \triangleq \mathbf{j}_n$ , (3) can be simplified to

$$\mathbf{e}_m = \mathbf{H}_{mn} \mathbf{j}_n + s_R \mathbf{w}_m, \quad (4)$$

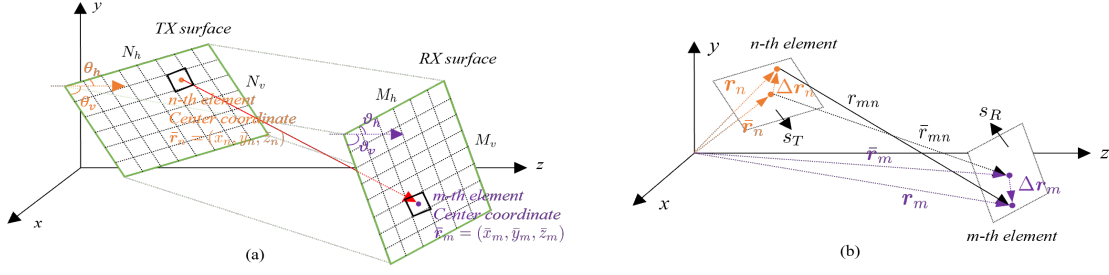


Fig. 1: (a) Demonstration of arbitrarily placed TX and RX surfaces in Cartesian coordinates. (b) Demonstration of the  $n$ -th TX element and the  $m$ -th RX element.

where the exact near-field LoS channel  $\mathbf{H}_{mn}$  is defined as

$$\mathbf{H}_{mn} = \frac{\eta}{2\lambda} \int_{s_R} \int_{s_T} \mathbf{G}(\mathbf{r}_m, \mathbf{t}_n) dt_n d\mathbf{r}_m. \quad (5)$$

It is observed that the simplified input-output model (4) provides an explicit representation of the communication link between the  $mn$ -pair.

We extend the basic model (4) to the whole H-MIMO system by embedding  $\mathbf{H}_{mn}$  as the  $(m, n)$ -th element of the overall H-MIMO channel matrix. As such, the relation between the imposed current distributions of all TX antenna elements to the measured electric fields of all RX antenna elements can be obtained as

$$\mathbf{e} = \mathbf{H}\mathbf{j} + s_R \mathbf{w}, \quad (6)$$

where  $\mathbf{e} = [e_1, e_2, \dots, e_M]^T$  represents the vector of all measured electric fields with each element given by  $e_m = [e_m^x, e_m^y, e_m^z]^T$ ;  $\mathbf{w} = [\mathbf{w}_1, \mathbf{w}_2, \dots, \mathbf{w}_N]^T$  denotes the additive white Gaussian noise vector, where  $\mathbf{w}_n = [w_n^x, w_n^y, w_n^z]^T$ ;  $\mathbf{j} = [\mathbf{j}_1, \mathbf{j}_2, \dots, \mathbf{j}_N]^T$  is the vector of imposed current distributions with elements  $\mathbf{j}_n = [j_n^x, j_n^y, j_n^z]^T$ ; and

$$\mathbf{H} = \begin{bmatrix} \mathbf{H}_{11} & \mathbf{H}_{12} & \cdots & \mathbf{H}_{1N} \\ \mathbf{H}_{21} & \mathbf{H}_{22} & \cdots & \mathbf{H}_{2N} \\ \vdots & \vdots & \ddots & \vdots \\ \mathbf{H}_{M1} & \mathbf{H}_{M2} & \cdots & \mathbf{H}_{MN} \end{bmatrix} \quad (7)$$

with each element matrix given by (5).

### B. Arbitrariness of Surface Placements

It is well-known that a surface located in the Cartesian coordinate system can be fully characterized by any two unit vectors belonging to it, and its center coordinates. Any vector



located on this surface can be represented using these unit vectors. The arbitrariness of surface placements can be completely controlled by these two unit vectors and the center coordinates.

Without loss of generality, we apply the horizontal unit vector and the vertical unit vector of the surface as those two unit vectors, and define them for the TX surface as

$$\mathbf{t}_T^h = [\sin \theta_h \cos \phi_h \quad \sin \theta_h \sin \phi_h \quad \cos \theta_h]^T, \quad (8)$$

$$\mathbf{t}_T^v = [\sin \theta_v \cos \phi_v \quad \sin \theta_v \sin \phi_v \quad \cos \theta_v]^T, \quad (9)$$

where  $\theta_h$  and  $\theta_v$  are the polar angles of the horizontal direction and the vertical direction of the TX surface, respectively, i.e., the angle between the  $z$ -axis and the horizontal/vertical direction of the TX surface as shown in Fig. 1(a);  $\phi_h$  and  $\phi_v$  are the azimuth angles of the horizontal direction and the vertical direction of the TX surface, respectively, namely, the angle between  $x$ -axis and  $xy$ -plane projection of the horizontal/vertical direction. Likewise, we define the horizontal unit vector and the vertical unit vector for the RX surface as

$$\mathbf{r}_R^h = [\sin \vartheta_h \cos \psi_h \quad \sin \vartheta_h \sin \psi_h \quad \cos \vartheta_h]^T, \quad (10)$$

$$\mathbf{r}_R^v = [\sin \vartheta_v \cos \psi_v \quad \sin \vartheta_v \sin \psi_v \quad \cos \vartheta_v]^T, \quad (11)$$

where  $\vartheta_h$ ,  $\vartheta_v$ ,  $\psi_h$ , and  $\psi_v$  are the polar angles and the azimuth angles defined for the RX surface. These defined angle parameters are capable of controlling the orientation of antenna surfaces. It is worth noting that they also control the surface shape (and of course the element shape). The following lemma provides the condition that guarantees the surface shape (element shape) to be rectangle (or square), otherwise, the surface shape (element shape) becomes diamond.

**Lemma 1.** *For the TX/RX surface with its horizontal unit vector and vertical unit vector given by (8), (10) and (9), (11), the TX/RX surface and their elements are guaranteed to be rectangle (or square) if and only if*

$$\begin{cases} \theta_h = 90^\circ \text{ or } \theta_v = 90^\circ, & \text{for TX,} \\ \vartheta_h = 90^\circ \text{ or } \vartheta_v = 90^\circ, & \text{for RX,} \end{cases} \quad (12)$$

*Proof.* See appendix A. □

Next, we present the representation of an arbitrary point located on the TX/RX surface via using the center coordinates. Since the surfaces are divided into discrete antenna elements, an arbitrary point located on the surfaces should belong to a certain antenna element. Without loss

of generality, we select the  $n$ -th antenna element of TX and the  $m$ -th antenna element of RX, depicted by their center coordinates  $\bar{\mathbf{t}}_n = [\bar{x}_n, \bar{y}_n, \bar{z}_n]^T$  and  $\bar{\mathbf{r}}_m = [\bar{x}_m, \bar{y}_m, \bar{z}_m]^T$ , respectively. Let  $\mathbf{t}_n$  and  $\mathbf{r}_m$  be arbitrary points belonging to the  $n$ -th TX antenna element and the  $m$ -th RX antenna element, respectively. It is obvious that  $\mathbf{t}_n$  and  $\mathbf{r}_m$  lie in the nearby regions of  $\bar{\mathbf{t}}_n$  and  $\bar{\mathbf{r}}_m$ , and are within  $s_T$  and  $s_R$ , respectively, as demonstrated in Fig. 1(b). Therefore, we have

$$\mathbf{t}_n = \bar{\mathbf{t}}_n + \Delta\mathbf{t}_n, \quad (13)$$

$$\mathbf{r}_m = \bar{\mathbf{r}}_m + \Delta\mathbf{r}_m, \quad (14)$$

where  $\Delta\mathbf{t}_n \triangleq [\Delta x_n \ \Delta y_n \ \Delta z_n]^T$  and  $\Delta\mathbf{r}_m \triangleq [\Delta x_m \ \Delta y_m \ \Delta z_m]^T$  belong to  $s_T$  and  $s_R$ , respectively. Accordingly, any arbitrary point within the TX/RX surface can be demonstrated by the center coordinates of a certain antenna element. More importantly, the  $\Delta z$  component ( $\Delta z_n$  and  $\Delta z_m$ ) is determined by  $\Delta x$  ( $\Delta x_n$  and  $\Delta x_m$ ) and  $\Delta y$  ( $\Delta y_n$  and  $\Delta y_m$ ) according to the coplanar restriction. The following lemma unveils their connections, which will be utilized in the following near-field LoS channel modeling.

**Lemma 2.** *Suppose TX and RX antenna elements with area  $s_T$  and area  $s_R$  are located in the Cartesian coordinate system, with their horizontal unit vector and vertical unit vector given by (8) (9) and (10) (11), respectively. For any arbitrary point  $\Delta\mathbf{t}_n \in s_T$  and any arbitrary point  $\Delta\mathbf{r}_m \in s_R$ , their  $\Delta z$  components can be represented by the  $\Delta x$  component and the  $\Delta y$  component, respectively, as*

$$\Delta z_n = \frac{\cot \theta_v \sin \phi_h - \cot \theta_h \sin \phi_v}{\sin(\phi_h - \phi_v)} \Delta x_n + \frac{\cot \theta_v \cos \phi_h - \cot \theta_h \cos \phi_v}{\sin(\phi_h - \phi_v)} \Delta y_n, \quad (15)$$

$$\Delta z_m = \frac{\cot \vartheta_v \sin \psi_h - \cot \vartheta_h \sin \psi_v}{\sin(\psi_h - \psi_v)} \Delta x_m + \frac{\cot \vartheta_v \cos \psi_h - \cot \vartheta_h \cos \psi_v}{\sin(\psi_h - \psi_v)} \Delta y_m. \quad (16)$$

*Proof.* See appendix B. □

It is remarkable that Lemma 2 provides the results without restricting the surface shape to be diamond or rectangle (square). If the rectangle (square) shape is chosen,  $\theta_h$  or  $\theta_v$  for TX and  $\vartheta_h$  or  $\vartheta_v$  for RX should be  $90^\circ$ . Meanwhile,  $\phi_h - \phi_v = 90^\circ$  and  $\psi_h - \psi_v = 90^\circ$  hold as well. As a result,  $\Delta z_n$  and  $\Delta z_m$  reduce to more compact forms, where we omit this for brevity.

### III. EM-DOMAIN NEAR-FIELD LOS CHANNEL MODELING

As seen from the channel expression derived in previous section that the near-field LoS channel is depicted by integrals of the tensor Green's function, which is implicit and computationally

infeasible, especially for obtaining the channel matrix (7) of an H-MIMO system with nearly infinite antenna elements. To mitigate the gap, in the following of this section, we propose to derive an explicit expression of the channel by eliminating the integral operators. We take advantage of our effective representation approach for surface placements, and exploit the Taylor series expansion to tackle the problem. As a consequence, a CD-CM, relying on the absolute coordinates of antenna element locations, is first derived, which shows a good approximation to the exact channel model (demonstrated in numerical evaluations below). Using a reasonable approximation, this model is further simplified to a concise CI-CM with an acceptable precision sacrifice. This concise model only relies on the relative locations of antenna elements, paying the way for its wide applications.

To achieve the goal, an explicit expression of the tensor Green's function is employed [29]

$$\mathbf{G}(\mathbf{r}_m, \mathbf{t}_n) = \frac{-ie^{ik_0 d_{mn}}}{4\pi d_{mn}} \left[ \left( 1 + \frac{i}{k_0 d_{mn}} - \frac{1}{k_0^2 d_{mn}^2} \right) \mathbf{I}_3 + \left( \frac{3}{k_0^2 d_{mn}^2} - \frac{3i}{k_0 d_{mn}} - 1 \right) \frac{\mathbf{d}_{mn} \mathbf{d}_{mn}^T}{d_{mn}^2} \right]. \quad (17)$$

As previously shown in (13) and (14),  $\mathbf{t}_n$  and  $\mathbf{r}_m$  are located at nearby regions (i.e., area  $s_T$  and area  $s_R$ , respectively) of  $\bar{\mathbf{t}}_n$  and  $\bar{\mathbf{r}}_m$ , respectively. The distance between  $\mathbf{t}_n$  and  $\mathbf{r}_m$  is determined accordingly as  $d_{mn} = \|\bar{\mathbf{r}}_m - \bar{\mathbf{t}}_n + \Delta\mathbf{r}_m - \Delta\mathbf{t}_n\|_2$ . Since both transmit and receive antenna elements are infinitesimal compared to the distance between them,  $d_{mn}$  can therefore be approximated by the distance between the area centers, namely,  $\bar{d}_{mn} \triangleq \|\bar{\mathbf{d}}_{mn}\|_2 = \|\bar{\mathbf{r}}_m - \bar{\mathbf{t}}_n\|_2$ . We use this approximation to the amplitude term of tensor Green's function and keep its phase term unchanged, yielding the approximated tensor Green's function

$$\mathbf{G}(\mathbf{r}_m, \mathbf{t}_n) \approx \mathbf{A}_{mn} \cdot e^{ik_0 \|\bar{\mathbf{r}}_m - \bar{\mathbf{t}}_n + \Delta\mathbf{r}_m - \Delta\mathbf{t}_n\|_2}, \quad (18)$$

where the approximated amplitude term is given by

$$\mathbf{A}_{mn} = \frac{-i}{4\pi \bar{d}_{mn}} \left[ \left( 1 + \frac{i}{k_0 \bar{d}_{mn}} - \frac{1}{k_0^2 \bar{d}_{mn}^2} \right) \mathbf{I}_3 + \left( \frac{3}{k_0^2 \bar{d}_{mn}^2} - \frac{3i}{k_0 \bar{d}_{mn}} - 1 \right) \frac{\bar{\mathbf{d}}_{mn} \bar{\mathbf{d}}_{mn}^T}{\bar{d}_{mn}^2} \right].$$

In deriving  $\mathbf{H}_{mn}$ , one can directly observe that the approximated amplitude  $\mathbf{A}_{mn}$  of tensor Green's function can be extracted outside the integrals, thereby resulting in

$$\mathbf{H}_{mn} \approx \frac{\eta}{2\lambda} \cdot \mathbf{A}_{mn} \int_{s_R} \int_{s_T} e^{ik_0 \|\bar{\mathbf{r}}_m - \bar{\mathbf{t}}_n + \Delta\mathbf{r}_m - \Delta\mathbf{t}_n\|_2} \cdot d\Delta\mathbf{t}_n d\Delta\mathbf{r}_m. \quad (19)$$

In order to further proceed with the integrals, we resort to the Taylor series expansion, which states that a scalar function  $f(\mathbf{x}_0 + \mathbf{x})$  can be expanded as  $f(\mathbf{x}_0 + \mathbf{x}) = f(\mathbf{x}_0) + \nabla f(\mathbf{x}_0)^T \mathbf{x} +$

$\frac{1}{2}\mathbf{x}^T\nabla^2 f(\mathbf{x}_0)\mathbf{x} + o(\|\mathbf{x}\|_2^2)$ , where  $o(\cdot)$  denotes the high-order terms. As such, we can expand the distance  $d_{mn}$  accordingly and obtain its approximation as

$$\begin{aligned} d_{mn} &= \bar{d}_{mn} + \frac{\bar{\mathbf{d}}_{mn}^T}{\bar{d}_{mn}}(\Delta\mathbf{r}_m - \Delta\mathbf{t}_n) + \frac{1}{2}(\Delta\mathbf{r}_m - \Delta\mathbf{t}_n)^T \mathcal{H}(\Delta\mathbf{r}_m - \Delta\mathbf{t}_n) + o(\|\Delta\mathbf{r}_m - \Delta\mathbf{t}_n\|_2^2) \\ &\approx \bar{d}_{mn} + \frac{\bar{\mathbf{d}}_{mn}^T}{\bar{d}_{mn}}(\Delta\mathbf{r}_m - \Delta\mathbf{t}_n), \end{aligned} \quad (20)$$

where  $\mathcal{H} = \nabla^2\|\bar{\mathbf{r}}_m - \bar{\mathbf{t}}_n\|_2$  denotes the Hessian matrix. The approximation in (20) holds by eliminating the second-order and high-order terms of the expansion, which is reasonable as they can be neglected for infinitesimal antenna elements. Substituting (20) back into (19), we get

$$\mathbf{H}_{mn} \approx \frac{\eta}{2\lambda} \mathbf{A}_{mn} e^{ik_0\bar{d}_{mn}} \int_{s_R} e^{ik_0\frac{\bar{\mathbf{d}}_{mn}^T}{\bar{d}_{mn}}\Delta\mathbf{r}_m} d\Delta\mathbf{r}_m \int_{s_T} e^{-ik_0\frac{\bar{\mathbf{d}}_{mn}^T}{\bar{d}_{mn}}\Delta\mathbf{t}_n} d\Delta\mathbf{t}_n \triangleq \frac{\eta}{2\lambda} \mathbf{A}_{mn} e^{ik_0\bar{d}_{mn}} I_R I_T, \quad (21)$$

where the double integrals are decomposed into two individual integrals,  $I_T$  and  $I_R$ .

#### A. Coordinate-Dependent Channel Model (CD-CM)

It is worth noting that the integral regions of  $I_T$  and  $I_R$  are restricted to their corresponding element surface areas, respectively, which does not correspond to the volume property of  $d\Delta\mathbf{t}_n$  and  $d\Delta\mathbf{r}_m$  in a point to point manner. Lemma 2 allows us to tackle the problem stated previously in a non-point-to-point manner, facilitating the derivations of  $I_T$  and  $I_R$ . One can obtain  $\mathbf{H}_{mn}$  by plugging them back into (21). The following theorem demonstrates our derived result.

**Theorem 1.** *For communications occurred between an  $M$ -element TX surface and an  $N$ -element RX surface, both located in the Cartesian coordinate system with arbitrary placements, and each surface comprises antenna elements with an equal element area,  $s_T$  and  $s_R$  for TX and RX, respectively, the near-field LoS channel for the  $mn$ -pair is established as*

$$\mathbf{H}_{mn} \approx \frac{\eta}{2\lambda} \cdot (l_R^h l_R^v) \cdot (l_T^h l_T^v) \cdot \mathbf{A}_{mn} \cdot e^{ik_0\bar{d}_{mn}} \cdot \varrho_{mn}, \quad (22)$$

where the factor  $\varrho_{mn}$  is given by

$$\begin{aligned} \varrho_{mn} &= \text{sinc} \left[ \frac{\pi l_T^h \bar{x}_{mn} + \bar{z}_{mn} \frac{\sin\phi_h \cot\theta_v - \sin\phi_v \cot\theta_h}{\sin(\phi_h - \phi_v)}}{\lambda \bar{d}_{mn}} \right] \text{sinc} \left[ \frac{\pi l_T^v \bar{y}_{mn} + \bar{z}_{mn} \frac{\cos\phi_h \cot\theta_v - \cos\phi_v \cot\theta_h}{\sin(\phi_h - \phi_v)}}{\lambda \bar{d}_{mn}} \right] \times \\ &\text{sinc} \left[ \frac{\pi l_R^h \bar{x}_{mn} + \bar{z}_{mn} \frac{\sin\psi_h \cot\vartheta_v - \sin\psi_v \cot\vartheta_h}{\sin(\psi_h - \psi_v)}}{\lambda \bar{d}_{mn}} \right] \text{sinc} \left[ \frac{\pi l_R^v \bar{y}_{mn} + \bar{z}_{mn} \frac{\cos\psi_h \cot\vartheta_v - \cos\psi_v \cot\vartheta_h}{\sin(\psi_h - \psi_v)}}{\lambda \bar{d}_{mn}} \right]. \end{aligned} \quad (23)$$

*Proof.* See appendix C. □

Theorem 1 provides a generalized channel model for both diamond and rectangle (square) surfaces. The result can be specific to the rectangle (square) surface setup, given by

$$\mathbf{H}_{mn} \approx \frac{\eta}{2\lambda} \cdot s_R s_T \cdot \mathbf{A}_{mn} \cdot e^{ik_0 \bar{d}_{mn}} \cdot \varrho_{mn}, \quad (24)$$

where  $s_T = l_T^h l_T^v$ ,  $s_R = l_R^h l_R^v$ , and the factor  $\varrho_{mn}$  becomes a reduced expression accordingly in cases when  $(\theta_h = 90^\circ \text{ and } \vartheta_h = 90^\circ)$  or  $(\theta_h = 90^\circ \text{ and } \vartheta_v = 90^\circ)$  or  $(\theta_v = 90^\circ \text{ and } \vartheta_h = 90^\circ)$  or  $(\theta_v = 90^\circ \text{ and } \vartheta_v = 90^\circ)$ , which we omit the expressions for brevity.

*Remark:* Compared with the exact channel model (5), our approximated channel model (24) eliminates the integral operators and provides an explicit and computationally-efficient surrogate. This approximated model shows that the  $mn$ -pair channel can be depicted by the distance between their area centers, their surface areas, as well as the angles of their surface placements. We also point out that this model relies on the absolute location coordinates of the antenna element center in deriving  $\bar{x}_{mn}$ ,  $\bar{y}_{mn}$  and  $\bar{z}_{mn}$ . Moreover, It is remarkable that the channel model in (24) generalizes the conventional parallel placement channel model established in [19]. Specifically, when the TX and RX surfaces are parallel to each other, and are also placed parallel to the  $xy$ -plane, the polar angles  $\theta_h$ ,  $\theta_v$ ,  $\vartheta_h$ , and  $\vartheta_v$  will be  $90^\circ$ , and the terms including  $\bar{z}_{mn}$  will reduce to zero, resulting in the channel model derived in [19].

### B. Coordinate-Independent Channel Model (CI-CM)

The CD-CM shows an excellent approximation to the exact channel (shown in numerical evaluations). It is however sophisticated in its expression for further applications, and also requires the concrete coordinates of each antenna element, which is possibly impractical in many cases. Instead, we may aware of the relative distance and direction between TX and RX antenna elements. As such, it is essential to develop a concise coordinate-independent but effective alternative, presented by the following corollary.

**Corollary 1.** *Consider communications between a rectangle  $M$ -element TX surface with an area of  $s_T$  and a rectangle  $N$ -element RX surface with an area of  $s_R$ . The near-field LoS channel between each  $mn$ -pair is simplified to a coordinate-independent alternative, given by*

$$\mathbf{H}_{mn} \approx \frac{\eta}{2\lambda} s_R s_T \mathbf{A}_{mn} e^{ik_0 \bar{d}_{mn}} = \frac{\eta}{2\lambda} s_R s_T \mathbf{G}(\bar{\mathbf{d}}_{mn}). \quad (25)$$

*Proof.* To relieve the dependency on the absolute location coordinates, we resort to the Taylor series expansion to the  $\text{sinc}(x)$  function, namely,  $\text{sinc}(x) = 1 - \frac{x^2}{3!} + \frac{x^4}{5!} - \frac{x^6}{7!} + \dots = \sum_{q=0}^{\infty} \frac{(-1)^q x^{2q}}{(2q+1)!}$ .

We notice that, for infinitesimal antenna elements, the high-order terms in the expansion can be neglected, especially when several sinc functions multiplying with each other. We thus get

$$\varrho_{mn} \approx 1 - \frac{\left[ \frac{\pi l_T^h}{\lambda} \bar{x}_{mn} + \bar{z}_{mn} \frac{\sin \phi_h \cot \theta_v - \sin \phi_v \cot \theta_h}{\sin(\phi_h - \phi_v)} \right]^2}{3!} - \frac{\left[ \frac{\pi l_T^v}{\lambda} \bar{y}_{mn} + \bar{z}_{mn} \frac{\cos \phi_h \cot \theta_v - \cos \phi_v \cot \theta_h}{\sin(\phi_h - \phi_v)} \right]^2}{3!} - \frac{\left[ \frac{\pi l_R^h}{\lambda} \bar{x}_{mn} + \bar{z}_{mn} \frac{\sin \psi_h \cot \vartheta_v - \sin \psi_v \cot \vartheta_h}{\sin(\psi_h - \psi_v)} \right]^2}{3!} - \frac{\left[ \frac{\pi l_R^v}{\lambda} \bar{y}_{mn} + \bar{z}_{mn} \frac{\cos \psi_h \cot \vartheta_v - \cos \psi_v \cot \vartheta_h}{\sin(\psi_h - \psi_v)} \right]^2}{3!} \approx 1. \quad (26)$$

Substituting the result to (24), we obtain the expected result, which completes the proof.  $\square$

To explicitly demonstrate the reasonability, we provide the following numerical example, in which we assume  $\bar{x}_{mn} = \bar{y}_{mn} = 0$  for brevity, such that  $\bar{d}_{mn} = \bar{z}_{mn}$ . We further set  $\phi_h = \psi_h = 90^\circ$ ,  $\phi_v = \psi_v = 0^\circ$ ,  $\theta_h = \theta_v = \vartheta_h = 90^\circ$ ,  $\vartheta_v = 60^\circ$ , implying that the angle between the TX and RX surfaces is  $30^\circ$ . Therefore,  $\frac{\sin \phi_h \cot \theta_v - \sin \phi_v \cot \theta_h}{\sin(\phi_h - \phi_v)} = 0$ ,  $\frac{\sin \psi_h \cot \vartheta_v - \sin \psi_v \cot \vartheta_h}{\sin(\psi_h - \psi_v)} = \frac{\sqrt{3}}{3}$  and  $\frac{\cos \phi_h \cot \theta_v - \cos \phi_v \cot \theta_h}{\sin(\phi_h - \phi_v)} = \frac{\cos \psi_h \cot \vartheta_v - \cos \psi_v \cot \vartheta_h}{\sin(\psi_h - \psi_v)} = 0$ . Since both TX and RX surfaces are nearly continuous, we make a moderate assumption that  $l_T^h = l_T^v = l_R^h = l_R^v = \frac{\lambda}{5}$ . Under these setups, we can calculate  $\varrho_{mn} = 0.978$ , which approximates to 1 with a negligible error.

It can be observed from (25) that the near-field LoS channel between  $mn$ -pair can be depicted by their surface areas, and the tensor Green's function in terms of their center distance  $\bar{d}_{mn}$  and the direction (unit vector)  $\bar{\mathbf{d}}_{mn}/\bar{d}_{mn}$ . Note that  $\bar{d}_{mn}$  and  $\bar{\mathbf{d}}_{mn}/\bar{d}_{mn}$  are irrelevant to the absolute coordinates of each antenna element, which can be acquired by distance and angle measurements.

#### IV. EM-DOMAIN CAPACITY LIMIT

Based upon our established near-field LoS channel model, it is capable of analyzing the capacity limit of the H-MIMO system from the EM-domain perspective. To realize this goal, we first build an effective analytical framework, where the EM-domain transmit and receive patterns (see Definition 1 below) are defined and introduced into the communication model, and an effective channel decomposition is then built for facilitating the analysis. We then unveil the fundamental capacity limit based upon this analytical framework in a rigorous derivation.

##### A. Transmit and Receive Patterns

For the purpose of rigorously formulating the communication model with transmit and receive patterns, and performing analysis on the fundamental limit, we first present the following definitions of the transmit and receive patterns.

**Definition 1.** The transmit or receive patterns of an H-MIMO communication system indicate a set of completed orthogonal bases  $\{\boldsymbol{\tau}_1(\mathbf{r}), \boldsymbol{\tau}_2(\mathbf{r}), \dots, \boldsymbol{\tau}_P(\mathbf{r})\}$  with  $\boldsymbol{\tau}_p(\mathbf{r}) = [\tau_p^x(\mathbf{r}), \tau_p^y(\mathbf{r}), \tau_p^z(\mathbf{r})]^T$  defined on the surface area  $\mathbf{r} \in S$ , capable of representing any arbitrary function defined on this surface area [26], [27], such as the current distribution  $\mathbf{j}$  or the electric field  $\mathbf{e}$ , namely,

$$\mathbf{o}(\mathbf{r}) = \sum_{p=1}^P \omega_p \boldsymbol{\tau}_p(\mathbf{r}), \quad \mathbf{o} \in \{\mathbf{j}, \mathbf{e}\}, \quad (27)$$

where  $\omega_p$  corresponds to the weight of each basis vector. Particularly, orthogonality holds

$$\int_A \boldsymbol{\tau}_p^H(\mathbf{r}) \boldsymbol{\tau}_q(\mathbf{r}) d\mathbf{r} = \delta_{pq}, \quad (28)$$

where  $\delta_{pq}$  is the Dirac delta function, given by  $\delta_{pq} = 1$  when  $p = q$  while  $\delta_{pq} = 0$  otherwise.

Following this definition, we denote the transmit patterns by  $\mathcal{S}_u = \{\mathbf{u}_1(\bar{\mathbf{t}}_n), \mathbf{u}_2(\bar{\mathbf{t}}_n), \dots, \mathbf{u}_P(\bar{\mathbf{t}}_n)\}$  on the area of the TX surface  $A_T$ , capable of generating the current distribution intended to be radiated. Likewise, we define the receive patterns by  $\mathcal{S}_v = \{\mathbf{v}_1(\bar{\mathbf{r}}_m), \mathbf{v}_2(\bar{\mathbf{r}}_m), \dots, \mathbf{v}_Q(\bar{\mathbf{r}}_m)\}$  on the area of the RX surface  $A_R$  to represent the measured electric field. Consequently, we get

$$\mathbf{j}_n(\bar{\mathbf{t}}_n) = \sum_{p=1}^P a_p \mathbf{u}_p(\bar{\mathbf{t}}_n), \quad (29)$$

$$\mathbf{e}(\bar{\mathbf{r}}_m) = \sum_{q=1}^Q c_q \mathbf{v}_q(\bar{\mathbf{r}}_m), \quad (30)$$

where  $a_p$  and  $c_q$  are the corresponding scalar weights. It is noteworthy that  $a_p$  and  $c_q$  can be the transmit symbol and the estimated receive symbol, respectively. In this regards,  $P$  equals  $Q$ , and both indicate the number of symbol streams. Based upon the representation by patterns, we establish the communication model of H-MIMO systems between the transmit and receive symbols. To assist the system modeling, we define the transmit and receive pattern matrices as

$$\mathbf{T} = \begin{bmatrix} \mathbf{u}_1(\bar{\mathbf{t}}_1) & \mathbf{u}_2(\bar{\mathbf{t}}_1) & \cdots & \mathbf{u}_P(\bar{\mathbf{t}}_1) \\ \mathbf{u}_1(\bar{\mathbf{t}}_2) & \mathbf{u}_2(\bar{\mathbf{t}}_2) & \cdots & \mathbf{u}_P(\bar{\mathbf{t}}_2) \\ \vdots & \vdots & \ddots & \vdots \\ \mathbf{u}_1(\bar{\mathbf{t}}_N) & \mathbf{u}_2(\bar{\mathbf{t}}_N) & \cdots & \mathbf{u}_P(\bar{\mathbf{t}}_N) \end{bmatrix}, \quad \mathbf{R} = \begin{bmatrix} \mathbf{v}_1(\bar{\mathbf{r}}_1) & \mathbf{v}_2(\bar{\mathbf{r}}_1) & \cdots & \mathbf{v}_Q(\bar{\mathbf{r}}_1) \\ \mathbf{v}_1(\bar{\mathbf{r}}_2) & \mathbf{v}_2(\bar{\mathbf{r}}_2) & \cdots & \mathbf{v}_Q(\bar{\mathbf{r}}_2) \\ \vdots & \vdots & \ddots & \vdots \\ \mathbf{v}_1(\bar{\mathbf{r}}_M) & \mathbf{v}_2(\bar{\mathbf{r}}_M) & \cdots & \mathbf{v}_Q(\bar{\mathbf{r}}_M) \end{bmatrix}, \quad (31)$$

based on which we obtain

$$\bar{\mathbf{j}} = \mathbf{T} \mathbf{a}, \quad (32)$$

$$\bar{\mathbf{e}} = \mathbf{R} \mathbf{c}, \quad (33)$$

where  $\mathbf{a} = [a_1, a_2, \dots, a_P]^T$  and  $\mathbf{c} = [c_1, c_2, \dots, c_Q]^T$  are the transmit and receive symbol vectors, respectively;  $\bar{\mathbf{j}} \triangleq [\mathbf{j}(\bar{\mathbf{t}}_1), \mathbf{j}(\bar{\mathbf{t}}_2), \dots, \mathbf{j}(\bar{\mathbf{t}}_N)]^T$  represents the vector consisting of current distributions at all  $N$  area centers of TX antenna elements;  $\bar{\mathbf{e}} \triangleq [\mathbf{e}(\bar{\mathbf{r}}_1), \mathbf{e}(\bar{\mathbf{r}}_2), \dots, \mathbf{e}(\bar{\mathbf{r}}_M)]^T$  denotes the vector consisting of electric fields at all  $M$  area centers of RX antenna elements.

The transmit and receive patterns have their own properties, relying on the following lemma.

**Lemma 3.** *Suppose that a surface area  $A$ , composing  $K$  uniformly divided small element areas  $S$ . Let  $\{\bar{\mathbf{r}}_1, \bar{\mathbf{r}}_2, \dots, \bar{\mathbf{r}}_K\}$  be the element centers. For a limited area surface with infinitesimal antenna elements, the integral of any two differentiable functions, defined on this surface area, can be well depicted using  $K$ ,  $S$  and the element centers, namely,*

$$\int_A \mathbf{f}^H(\mathbf{r})\mathbf{g}(\mathbf{r})d\mathbf{r} \approx S \sum_{k=1}^K \mathbf{f}^H(\bar{\mathbf{r}}_k)\mathbf{g}(\bar{\mathbf{r}}_k), \quad (34)$$

where  $\mathbf{f}(\mathbf{r})$  and  $\mathbf{g}(\mathbf{r})$  are those two differentiable functions defined on  $A$ .

*Proof.* See appendix D. □

Lemma 3 allows us to unveil the properties for the transmit and receive patterns, as well as the transmit and receive pattern matrices. It is stated by the following corollary.

**Corollary 2.** *For TX and RX surfaces with limited area and infinitesimal antenna elements, the transmit patterns  $\mathcal{S}_u = \{\mathbf{u}_1(\bar{\mathbf{t}}_n), \mathbf{u}_2(\bar{\mathbf{t}}_n), \dots, \mathbf{u}_P(\bar{\mathbf{t}}_n)\}$  defined on the area of TX surface  $A_T = N s_T$ , and the receive patterns  $\mathcal{S}_v = \{\mathbf{v}_1(\bar{\mathbf{r}}_m), \mathbf{v}_2(\bar{\mathbf{r}}_m), \dots, \mathbf{v}_Q(\bar{\mathbf{r}}_m)\}$  defined on the area of RX surface  $A_R = M s_R$ , nearly obey the orthogonality as follows*

$$\mathbf{T}^H \mathbf{T} \approx \frac{\mathbf{I}_P}{s_T}, \quad \mathbf{R}^H \mathbf{R} \approx \frac{\mathbf{I}_Q}{s_R}. \quad (35)$$

*Proof.* Based on Lemma 3, we approximate the pattern orthogonality (28) as

$$\delta_{pq} = \int_A \boldsymbol{\tau}_p^H(\mathbf{r})\boldsymbol{\tau}_q(\mathbf{r})d\mathbf{r} \approx S \sum_{k=1}^K \boldsymbol{\tau}_p^H(\bar{\mathbf{r}}_k)\boldsymbol{\tau}_q(\bar{\mathbf{r}}_k),$$

where  $A \in \{A_T, A_R\}$ ,  $\boldsymbol{\tau} \in \{\mathbf{u}, \mathbf{v}\}$ ,  $S \in \{s_T, s_R\}$ , and  $K \in \{N, M\}$ . By dividing  $S$  on both sides of the approximation, we derive (35), which completes the proof. □

Next, we integrate the transmit and receive patterns into the H-MIMO system model (6), where we rely on the established channel model (25) for brevity to derive the elements of the channel matrix. In addition, we connect  $\bar{\mathbf{j}}$  in (32) and  $\mathbf{j}$  in (6) based on the uniformly distributed assumption of the current distribution,  $\mathbf{j}_n = \mathbf{j}_n(\bar{\mathbf{t}}_n)$ , such that  $\mathbf{j} = \bar{\mathbf{j}}$ . Likewise, we bridge the



connection between  $\bar{e}$  in (33) and  $e$  in (6) via  $e_m = \int_{s_R} e(\mathbf{r}_m) d\mathbf{r}_m \approx s_R \cdot e(\bar{\mathbf{r}}_m)$  for infinitesimal area of the antenna elements, such that  $e \approx s_R \cdot \bar{e}$ . As a consequence, combining (6), (32), (33), we obtain the communication model using the pattern matrix property (35), yielding

$$\mathbf{c} = \frac{\eta}{2\lambda} \cdot s_R s_T \cdot \mathbf{R}^H \mathbf{G} \mathbf{T} \mathbf{a} + s_R \mathbf{R}^H \mathbf{w}, \quad (36)$$

where  $\mathbf{G}$  is specified to satisfy  $\mathbf{H} = \frac{\eta}{2\lambda} s_R s_T \mathbf{G}$ , and it will be detailed subsequently.

### B. Channel Decomposition

In building the communication model (36),  $\mathbf{G}$  is specified as a matrix composed of the tensor Green's function in terms of different center coordinates of TX/RX antenna elements. In particular, it is provided by

$$\mathbf{G} = \begin{bmatrix} \mathbf{G}(\bar{\mathbf{r}}_1, \bar{\mathbf{t}}_1) & \mathbf{G}(\bar{\mathbf{r}}_1, \bar{\mathbf{t}}_2) & \cdots & \mathbf{G}(\bar{\mathbf{r}}_1, \bar{\mathbf{t}}_N) \\ \mathbf{G}(\bar{\mathbf{r}}_2, \bar{\mathbf{t}}_1) & \mathbf{G}(\bar{\mathbf{r}}_2, \bar{\mathbf{t}}_2) & \cdots & \mathbf{G}(\bar{\mathbf{r}}_2, \bar{\mathbf{t}}_N) \\ \vdots & \vdots & \ddots & \vdots \\ \mathbf{G}(\bar{\mathbf{r}}_M, \bar{\mathbf{t}}_1) & \mathbf{G}(\bar{\mathbf{r}}_M, \bar{\mathbf{t}}_2) & \cdots & \mathbf{G}(\bar{\mathbf{r}}_M, \bar{\mathbf{t}}_N) \end{bmatrix}. \quad (37)$$

Since the defined transmit patterns  $\mathcal{S}_u$  and the receive patterns  $\mathcal{S}_v$  are completed orthogonal bases within area  $A_T$  and area  $A_R$ , respectively, the function of any arbitrary point belonging to each of the area can be formally represented by the corresponding orthogonal bases. Note that the tensor Green's function  $\mathbf{G}(\bar{\mathbf{r}}_m, \bar{\mathbf{t}}_n)$  is a function of  $\bar{\mathbf{t}}_n \in A_T$  and  $\bar{\mathbf{r}}_m \in A_R$ . Consequently, it can be decomposed using these orthogonal bases. More specifically, for a fixed  $\bar{\mathbf{r}}_m \in A_R$ ,  $\mathbf{G}(\bar{\mathbf{r}}_m, \bar{\mathbf{t}}_n)$  is merely a function of  $\bar{\mathbf{t}}_n \in A_T$ , which can thus be interpreted by  $\mathcal{S}_u$  as [27]

$$\mathbf{G}(\bar{\mathbf{r}}_m, \bar{\mathbf{t}}_n) = \sum_{p=1}^P \mathbf{h}_p(\bar{\mathbf{r}}_m) \mathbf{u}_p^H(\bar{\mathbf{t}}_n), \quad (38)$$

where  $\mathbf{h}_p(\bar{\mathbf{r}}_m) = \int_{A_T} \mathbf{G}(\bar{\mathbf{r}}_m, \mathbf{t}) \mathbf{u}_p(\mathbf{t}) d\mathbf{t}$ , and it can be approximated via Lemma 3 by

$$\mathbf{h}_p(\bar{\mathbf{r}}_m) \approx \sum_{n=1}^N s_T \cdot \mathbf{G}(\bar{\mathbf{r}}_m, \bar{\mathbf{t}}_n) \mathbf{u}_p(\bar{\mathbf{t}}_n). \quad (39)$$

Accordingly,  $\mathbf{h}_p(\bar{\mathbf{r}}_m)$  is a function of  $\bar{\mathbf{r}}_m \in A_R$ , and can be decomposed by  $\mathcal{S}_v$  as

$$\mathbf{h}_p(\bar{\mathbf{r}}_m) = \sum_{q=1}^Q \gamma_{pq} \mathbf{v}_q(\bar{\mathbf{r}}_m), \quad (40)$$

where  $\gamma_{pq} = \int_{A_R} \mathbf{v}_q^H(\mathbf{r}) \mathbf{h}_p(\mathbf{r}) d\mathbf{r}$ , and it can be further obtained using Lemma 3 as follows

$$\gamma_{pq} \approx s_R s_T \sum_{n=1}^N \sum_{m=1}^M \mathbf{v}_q^H(\bar{\mathbf{r}}_m) \mathbf{G}(\bar{\mathbf{r}}_m, \bar{\mathbf{t}}_n) \mathbf{u}_p(\bar{\mathbf{t}}_n). \quad (41)$$

Based upon the decomposition, we substitute (40) to (38) to derive the bilinear decomposition of  $\mathbf{G}(\bar{\mathbf{r}}_m, \bar{\mathbf{t}}_n)$  with respect to orthogonal bases  $\mathcal{S}_u$  and  $\mathcal{S}_v$  by

$$\mathbf{G}(\bar{\mathbf{r}}_m, \bar{\mathbf{t}}_n) = \sum_{p=1}^P \sum_{q=1}^Q \gamma_{pq} \mathbf{v}_q(\bar{\mathbf{r}}_m) \mathbf{u}_p^H(\bar{\mathbf{t}}_n). \quad (42)$$

By further substituting this bilinear decomposition into (37), we reformulate the  $\mathbf{G}$  matrix as

$$\mathbf{G} = \mathbf{RDT}^H, \quad (43)$$

where  $\mathbf{D}$  indicates a matrix incorporating the coefficients  $\gamma_{pq}$ .

Substituting (43) into (36), and exploiting (35), we reformulate the communication model as

$$\mathbf{c} = \frac{\eta}{2\lambda} \mathbf{D}\mathbf{a} + s_R \mathbf{R}^H \mathbf{w}, \quad (44)$$

Since in our H-MIMO communication system, the receive symbol vector  $\mathbf{c}$  is an estimate of the transmit symbol vector  $\mathbf{a}$ , therefore,  $P = Q$ , and  $\mathbf{D}$  should be a diagonal matrix such that the communication model (44) forms a point-to-point mapping between each element of  $\mathbf{c}$  and  $\mathbf{a}$ . As a consequence,  $\gamma_{pq} = 0$  for  $p \neq q$ , leading to the newly bilinear decomposition

$$\mathbf{G}(\bar{\mathbf{r}}_m, \bar{\mathbf{t}}_n) = \sum_{p=1}^P \gamma_{pp} \mathbf{v}_p(\bar{\mathbf{r}}_m) \mathbf{u}_p^H(\bar{\mathbf{t}}_n). \quad (45)$$

### C. EM-Domain Capacity Limit

The definition of transmit and receive patterns facilitates the modeling of the end-to-end communication system, which provides a feasible access for analyzing the capacity limit of H-MIMO systems with arbitrary surface placements. In a consistent way, the established decomposition of channel matrix allows us to proceed this analysis in a tractable manner.

Suppose that the average transmit power is  $\frac{\mathcal{P}_t}{P}$  with  $\mathcal{P}_t$  being the total transmit power. Then the capacity is derived based upon (43) as [30]

$$C = \log_2 \left( \left| \mathbf{I}_P + \mu \cdot \text{SNR} \cdot \mathbf{D}\mathbf{D}^H \right| \right), \quad (46)$$

where  $\mu = \frac{\eta^2}{4\lambda^2}$  and  $\text{SNR} = \frac{\mathcal{P}_t}{P s_R \sigma_w^2}$  denotes the average transmit signal-to-noise ratio (SNR) per unit area. Furthermore,  $\mu \cdot \text{SNR} \cdot \mathbf{D}\mathbf{D}^H$  indicates the average receive SNR per unit area. Exploiting the diagonal structure of  $\mathbf{D}$ , we can further obtain (46) as

$$C = \log_2 \left( \prod_{p=1}^P \left( 1 + \mu \cdot \text{SNR} \cdot \gamma_{pp}^2 \right) \right) = \sum_{p=1}^P \log_2 \left( 1 + \mu \cdot \text{SNR} \cdot \gamma_{pp}^2 \right). \quad (47)$$

As seen accordingly from the result, the capacity is influenced by the average receive SNR, the wavelength, and the channel related parameters,  $\eta$  and  $\gamma_{pp}$ . Since we do not put our emphasis on designing the patterns, it is thus not explicit to us what the pattern matrices are. As such,  $\gamma_{pp}$ , associating with those patterns, cannot be directly determined, and thereby failing to unveil the capacity limit. One can refer to [31], [32] for pattern design.

To mitigate the gap, we intend to transform the unknown  $\gamma_{pp}$  to some known replacements, based on which, we suggest the following theorem that states the capacity limit.

**Theorem 2.** *Suppose that an H-MIMO communication system transmit between surfaces with arbitrary surface placements, the near-field LoS channel model between each  $mn$ -pair is captured using (25), as well as the transmit and receive patterns that are designed by  $\mathbf{T}$  and  $\mathbf{R}$ . The capacity limit of such a system is derived as*

$$C \leq P \cdot \log_2 \left( 1 + \frac{\mu \cdot \text{SNR}}{P} \cdot s_R s_T \cdot \sum_{m=1}^M \sum_{n=1}^N \left( \frac{\varepsilon_1}{\bar{d}_{mn}^2} + \frac{\varepsilon_2}{\bar{d}_{mn}^4} + \frac{\varepsilon_3}{\bar{d}_{mn}^6} \right) \right), \quad (48)$$

where the coefficients are given by

$$\varepsilon_1 = \frac{1}{16\pi^2 k_0^0} \left[ 3 - \text{trace} \left( \frac{\bar{\mathbf{d}}_{mn} \bar{\mathbf{d}}_{mn}^T}{\bar{d}_{mn}^2} \right) \right], \quad (48a)$$

$$\varepsilon_2 = \frac{1}{16\pi^2 k_0^2} \left[ 5 \cdot \text{trace} \left( \frac{\bar{\mathbf{d}}_{mn} \bar{\mathbf{d}}_{mn}^T}{\bar{d}_{mn}^2} \right) - 3 \right], \quad (48b)$$

$$\varepsilon_3 = \frac{1}{16\pi^2 k_0^4} \left[ 3 \cdot \text{trace} \left( \frac{\bar{\mathbf{d}}_{mn} \bar{\mathbf{d}}_{mn}^T}{\bar{d}_{mn}^2} \right) + 3 \right]. \quad (48c)$$

*Proof.* See appendix E. □

*Remark:* It can be seen that the capacity limit grows logarithmically with the product of transmit element area  $s_T$ , receive element area  $s_R$ , and the combined effects of  $1/\bar{d}_{mn}^2$ ,  $1/\bar{d}_{mn}^4$ , and  $1/\bar{d}_{mn}^6$  over all  $M$  and  $N$  antenna elements. Alternatively, it decreases logarithmically with the combined effects of  $\bar{d}_{mn}^2$ ,  $\bar{d}_{mn}^4$ , and  $\bar{d}_{mn}^6$  over all  $M$  and  $N$  antenna elements. These powers of  $\bar{d}_{mn}$  serve as a guideline for system designs. Specifically,  $\bar{d}_{mn}^6$  dominates the capacity limit in near-field regions, whereas  $\bar{d}_{mn}^2$  primarily affects the capacity limit in far-field regions. This offers coarse but pragmatic estimates of the performance limits for practical systems.

The result can be generalized to far-field scenarios as a special case, which can reversely validate the effectiveness of our result. Those terms corresponding to  $\bar{d}_{mn}^4$ , and  $\bar{d}_{mn}^6$  tend to be attenuated in far-field regions. Furthermore, the center distance between each  $mn$ -pair,  $\bar{d}_{mn}$ , can be approximated to a common distance, denoted as  $d_0$ , irrelevant to index  $m$  and  $n$ , due to

$d_0 \gg \max\{A_T, A_R\}$ . The direction (or unit vector) of  $mn$ -pair,  $\bar{\mathbf{d}}_{mn}/\bar{d}_{mn}$ , tends to be unified to a certain common direction, represented by  $\boldsymbol{\kappa}$ . As a consequence, the capacity limit becomes

$$C \leq P \cdot \log_2 \left( 1 + \frac{\mu \cdot \text{SNR}}{P} \cdot \bar{\varepsilon}_1 \cdot \frac{A_R A_T}{d_0^2} \right), \quad (49)$$

where  $\bar{\varepsilon}_1$  is deduced from  $\varepsilon_1$  based on  $(\bar{\mathbf{d}}_{mn} \bar{\mathbf{d}}_{mn}^T) / \bar{d}_{mn}^2 \approx \boldsymbol{\kappa} \boldsymbol{\kappa}^T$  and  $\boldsymbol{\kappa}^T \boldsymbol{\kappa} = 1$ , given by

$$\bar{\varepsilon}_1 = \frac{1}{16\pi^2} [3 - \text{trace}(\boldsymbol{\kappa} \boldsymbol{\kappa}^T)] = \frac{1}{8\pi^2}, \quad (50)$$

$A_R = M s_R$  and  $A_T = N s_T$  are the overall surface area of RX and TX, respectively. It can be seen that the capacity limit in the far-field scenario grows logarithmically with the the transmit and receive surface areas,  $A_T$  and  $A_R$ , and it decreases logarithmically with the square of surface distance. This conclusion is consistent with those insights on degree-of-freedom and power coupling obtained in [25], [27].

## V. NUMERICAL EVALUATIONS

We present numerical evaluations in this section, in which we first demonstrate the accuracy of our established channel models in capturing the essence of the wireless channel, and we then exhibit the capacity limit of the H-MIMO system using our derived results.

### A. Channel Model Evaluation

In channel model evaluations, two metrics are mainly focused, namely, the normalized mean-squared errors (NMSEs) between our established channel models and the true wireless channel, and the eigenvalues of the channel matrix in capturing eigenmodes of the true wireless channel. The eigenvalues can exactly reveal the eigenmodes (number of available eigenvalues larger than some thresholds) of H-MIMO systems. Particularly, the NMSE is defined as

$$\text{NMSE} = \frac{\|\hat{\mathbf{H}} - \mathbf{H}\|_F^2}{\|\mathbf{H}\|_F^2}, \quad (51)$$

where  $\mathbf{H}$  and  $\hat{\mathbf{H}}$  are the exact channel matrix and the modeled channel matrix, respectively. Unless specifically stated, we focus on rectangle (square) surfaces, corresponding to the polar angles and the azimuth angles of TX and RX as  $\theta_h = \theta_v = 90^\circ$ ,  $\phi_h = 0^\circ$ ,  $\phi_v = 90^\circ$ , and  $\vartheta_h = 90^\circ$ ,  $\vartheta_v = \{60^\circ, 75^\circ, 90^\circ\}$ ,  $\psi_h = 0^\circ$ ,  $\psi_v = 90^\circ$ , respectively. Moreover, we specify:

- “Exact” indicates  $\mathbf{H}$  obtained via (5);
- “CD-CM” specifies  $\hat{\mathbf{H}}$  obtained via (24);

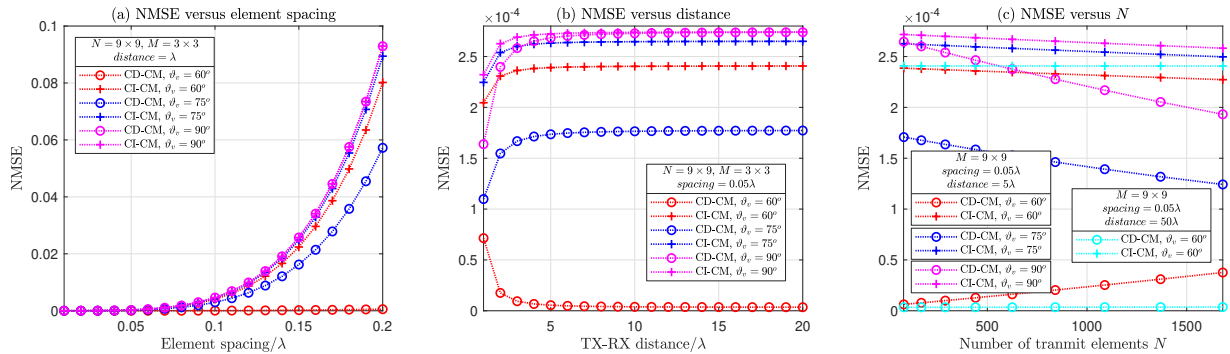


Fig. 2: NMSEs of established channel models versus (a) the element spacing of antenna surfaces, (b) the TX-RX distance, and (c) the number of transmit elements, respectively.

- “CI-CM” reveals  $\hat{\mathbf{H}}$  obtained via (25).

We provide numerical results with respect to element spacing, TX-RX distance, and the number of TX elements. Evaluations are tested at 30 GHz, corresponding to  $\lambda = 0.01$  meter wavelength.

We first present the NMSEs of our channel model with respect to the element spacing, shown in Fig. 2(a). In this evaluation, the number of transmit and receive elements are  $N = 9 \times 9$  and  $M = 3 \times 3$ , respectively. The TX-RX distance is set as  $\lambda$ . We have three observations from this figure: ① The NMSEs of CD-CM are always smaller than those of CI-CM, showing its better approximation to the true wireless channel. ② CD-CM and CI-CM become closely in NMSEs as  $\vartheta_v$  varying from  $60^\circ$  to  $90^\circ$ , namely as the TX-RX surfaces tending to be parallel. ③ As the element spacing becoming small, the NMSEs of CD-CM and CI-CM drastically decrease, showing a good agreement in capturing the nearly continuous surface induced H-MIMO channel.

Following the same settings while specifying the element spacing as  $0.05\lambda$ , we show NMSEs with respect to the TX-RX distance, ranging from  $\lambda$  to  $20\lambda$ , in Fig. 2(b). It can be seen that as the distance becoming large, the NMSEs of CD-CM and CI-CM tend to be flat, which are mainly restricted by the element spacing. In addition, CD-CM and CI-CM get closely in NMSEs for different  $\vartheta_v$  varying from  $60^\circ$  to  $90^\circ$ .

We further demonstrate NMSEs with respect to the number of transmit elements, as shown in Fig. 2(c). In this evaluation, we vary the number of transmit elements in the range of  $N \in [9 \times 9, 41 \times 41]$ , and fix the number of receive elements as  $M = 9 \times 9$ , under different TX-RX distances,  $5\lambda$  and  $50\lambda$ . We see from Fig. 2(c) that: ① The NMSEs of CD-CM are smaller than those of CI-CM for both distance cases, showing a better depiction of CD-CM once again. ②

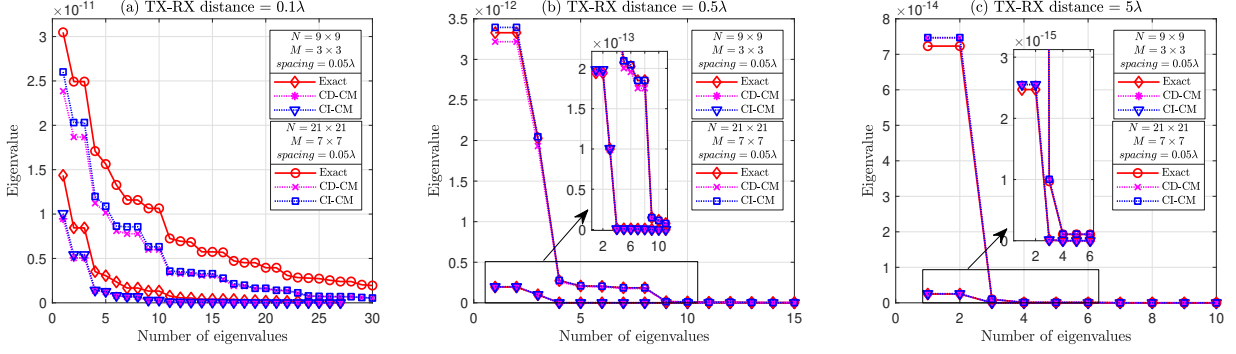


Fig. 3: Eigenvalue demonstration of channel matrices with respect to different transmit and receive elements at the TX-RX distance of (a)  $0.1\lambda$ , (b)  $0.5\lambda$ , and (c)  $5\lambda$ , respectively.

In the  $5\lambda$  case, when the TX and RX surfaces tend to be parallel ( $\vartheta_v = 75^\circ, 90^\circ$ ), NMSEs of CD-CM decrease as the number of transmit elements increases, while for a more non-parallel case ( $\vartheta_v = 60^\circ$ ), NMSEs of CD-CM increase slightly. ③ When the TX-RX distance is large enough (e.g.,  $50\lambda$ ), NMSEs of CD-CM appear to be flat with respect to  $N$ . ④ For all tested setups, the NMSEs of CI-CM become flat.

Next, we evaluate our channel models in depicting the eigenvalues of the true channel matrix. The element spacing is selected as  $0.05\lambda$ , and  $\vartheta_v$  is fixed as  $90^\circ$  with other angles kept unchanged. We test the number of transmit/receive elements as  $N = 9 \times 9$ ,  $M = 3 \times 3$  and  $N = 21 \times 21$ ,  $M = 7 \times 7$ , respectively. First, we observe from Fig. 3(a) that when the TX-RX distance is  $0.1\lambda$ , even if CD-CM and CI-CM fail to fit the exact channel in its eigenvalues, however, they can well capture the trend of eigenvalues as that of the exact channel. Afterwards, comparing among Fig. 3(a)(b)(c), as the TX-RX distance varying from  $0.1\lambda$  to  $0.5\lambda$  and  $5\lambda$ , we see that both CD-CM and CI-CM fit the exact channel well in eigenvalues and eigenmodes. Moreover, for shorter distances, more eigenmodes are introduced than those of longer distance, contributing to more independent transmission channels, even in LoS cases. From each individual demonstration of Fig. 3(a)(b)(c), we get that large number of transmit/receive elements facilitates more eigenmodes than that of small number of transmit/receive elements within a proper range of distance.

The above evaluations show the effectiveness of our channel models in capturing the essence of the true wireless channel.

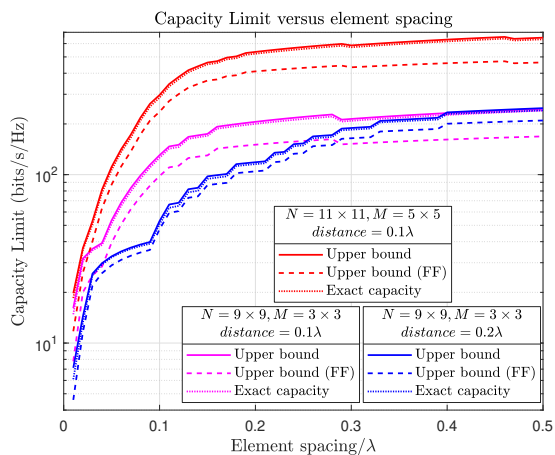
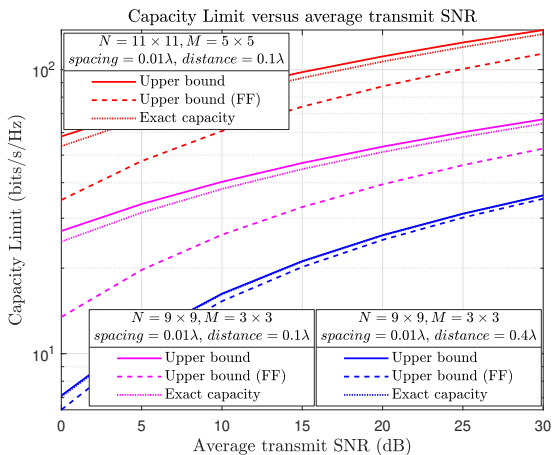


Fig. 4: Capacity limit versus TX average SNR. Fig. 5: Capacity limit versus element spacing.

### B. Capacity Limit Evaluation

In capacity limit evaluations, we focus on demonstrating the effectiveness and tightness of our derived upper bound in depicting the exact capacity limit. The numerical evaluations are performed in terms of the average transmit SNR, the element spacing, the TX-RX distance, and the number of transmit elements. Numerical assessments of the exact capacity (47) incorporate the evaluation of the unknown  $\gamma_{pp}$ , which needs to be addressed. For this purpose, we resort to the singular value decomposition via  $\mathbf{G} = \mathbf{U}\mathbf{\Sigma}\mathbf{V}^H$ , and set  $\mathbf{R} = \frac{\mathbf{U}(:,1:P)}{\sqrt{s_R}}$ ,  $\mathbf{T} = \frac{\mathbf{V}(:,1:P)}{\sqrt{s_T}}$ . As a consequence,  $\mathbf{D} = \sqrt{s_R s_T} \mathbf{\Sigma}(1:P, 1:P)$ , and  $\gamma_{pp}$  can be determined accordingly using singular values of  $\mathbf{\Sigma}$ . Moreover, we only select effective singular values from all noise corrupted ones, i.e., top- $P$  largest values, where  $P$  is determined adaptively when the top- $P$  values accounting for no lower than 80% power of all the singular values. We define “Upper bound” to indicate (48), and use “Upper bound (FF)” to specify (49) for the far-field case.

We check the capacity limit versus the average transmit SNR in Fig. 4, in which we present numerical results for different TX-RX distance ( $0.1\lambda$  and  $0.4\lambda$ ) under the same  $N = 9 \times 9$ ,  $M = 3 \times 3$ , as well as exhibit numerical results for a different  $N = 11 \times 11$ ,  $M = 5 \times 5$  at a TX-RX distance of  $0.1\lambda$ . In all cases, the element spacing is set as  $0.01\lambda$ . We first notice that the capacity is proportional to the SNR, and the “Upper bound” provides an effective and tightness bound for the exact capacity in all tested cases. Another notable phenomenon is that the “Upper bound (FF)” fails to offer a valid bound on the exact capacity, especially when the distance is small and falls in the near-field regions.

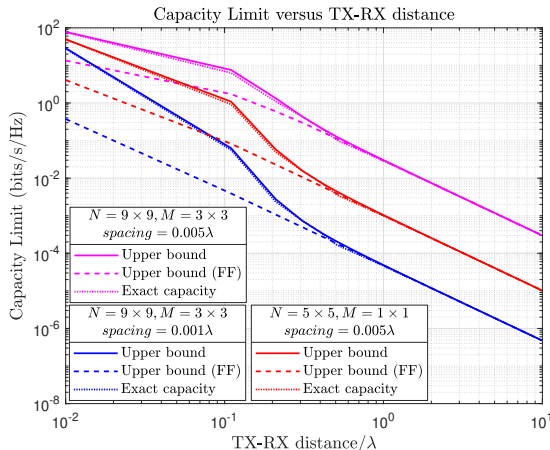
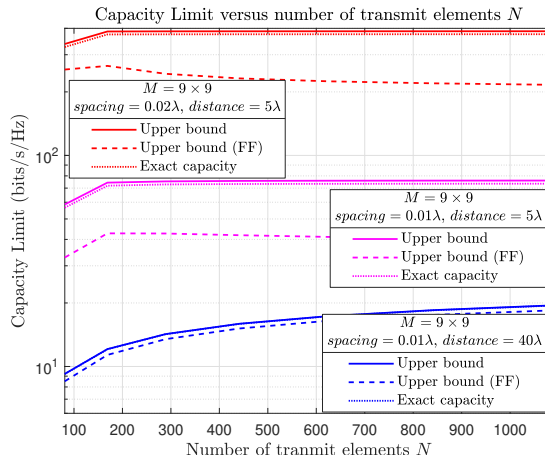


Fig. 6: Capacity limit versus TX-RX distance.

Fig. 7: Capacity limit versus  $N$ .

Subsequently, the capacity limit versus the element spacing is shown in Fig. 5, where we test the element spacing ranging from  $0.01\lambda$  to  $0.5\lambda$ , and apply the same setup in TX-RX distance,  $N$  and  $M$ , as those in Fig. 4. As we fix the number of transmit and receive elements, therefore, the element spacing determines the surface area, with a large/small element spacing corresponding to a large/small surface area. From the figure, we observe that the capacity increase for large element spacing, namely, large surface area enables large capacity. In addition, we once verify that, for all tested cases, “Upper bound” provides a tightness bound on the exact capacity limit, while “Upper bound (FF)” cannot capture the accurate upper bound and the exact capacity limit.

Furthermore, we unveil the capacity limit versus the TX-RX distance in Fig. 6, where cases for different element spacing ( $0.001\lambda$  and  $0.005\lambda$ ) under the same  $N = 9 \times 9$ ,  $M = 3 \times 3$ , and the case for  $N = 5 \times 5$ ,  $M = 1 \times 1$  with an element spacing of  $0.005\lambda$  are considered. It can be seen that, as the TX-RX distance becoming large, the capacity limits drop drastically. “Upper bound” successfully depicts the exact capacity limit within a negligible gap over the whole distance range, and it gradually collapses to the “Upper bound (FF)” as the TX-RX distance increases.

In the end, the influence of the number of transmit elements on capacity limit is exhibited in Fig. 7, where we fix  $M = 9 \times 9$  and vary  $N$  from  $9 \times 9$  to  $33 \times 33$  with element spacings  $\{0.01\lambda, 0.02\lambda\}$  at TX-RX distances  $\{5\lambda, 40\lambda\}$ . It can be seen that the exact capacity limit can be perfectly captured by the “Upper bound” in all setups. Moreover, the capacity limits for both element spacing and TX-RX distance cases gradually increase along with  $N$ , but tend to be flat at a certain inflection point, especially for the short distance  $5\lambda$ . This is mainly limited by small



*M.* Finally, both large surface area (compare red and pink curves) and short TX-RX distance (from blue to pink and red curves) promote high capacity limits.

Overall, the evaluations reveal that our derived capacity upper bound is effective and quite tight for depicting the real capacity limit. Besides, the large surface area and the short distance facilitate the increase in H-MIMO capacity.

## VI. CONCLUSIONS

In this article, we considered the point-to-point H-MIMO systems with arbitrary surface placements in a near-field LoS scenario, in which we established the generalized EM-domain near-field LoS channel models and studied the capacity limit. We first established effective, explicit, and computationally-efficient CD-CM and CI-CM, which are valid in approaching the exact near-field LoS channel and in capturing the essence of physical wireless channel, such as the degrees-of-freedom of channel matrix. We then built an effective analytical framework for deriving the capacity limit. We showed that the capacity limit grows logarithmically with the product of TX and RX element areas and the combined effects of  $1/\bar{d}_{mn}^2$ ,  $1/\bar{d}_{mn}^4$ , and  $1/\bar{d}_{mn}^6$  over all  $M$  and  $N$  antenna elements. Our result can exactly capture the exact capacity, offering an effective mean for predicting the system performance.

### APPENDIX A

#### PROOF OF LEMMA 1

Without loss of generality, we take the TX surface for example. Suppose that the TX surface has a horizontal length  $L_T^h$ , a vertical length  $L_T^v$ , and a diagonal length  $L_T$ , as shown in Fig. 8. The projections of horizontal and vertical lengths on the  $xy$ -plane are defined as  $\ell_T^h$  and  $\ell_T^v$ , respectively, which can be derived as  $\ell_T^h = L_T^h \sin \theta_h$  and  $\ell_T^v = L_T^v \sin \theta_v$ . Likewise, we can also obtain the projections of horizontal and vertical lengths on the  $z$ -axis as  $z_T^h = L_T^h \cos \theta_h$  and  $z_T^v = L_T^v \cos \theta_v$ . Therefore, we know that  $(L_T^h)^2 = (\ell_T^h)^2 + (z_T^h)^2$ , and  $(L_T^v)^2 = (\ell_T^v)^2 + (z_T^v)^2$ . Note that if the surface (and element) is rectangle (or square), the following equation should hold using the Pythagorean theorem

$$(L_T)^2 = (L_T^h)^2 + (L_T^v)^2 = (\ell_T^h)^2 + (L_T^h \cos \theta_h)^2 + (\ell_T^v)^2 + (L_T^v \cos \theta_v)^2.$$

Alternatively, we can express  $L_T$  as

$$(L_T)^2 = (\ell_T^h)^2 + (\ell_T^v)^2 + (z_T)^2 \stackrel{(1)}{=} (\ell_T^h)^2 + (\ell_T^v)^2 + (L_T^h \cos \theta_h + L_T^v \cos \theta_v)^2,$$

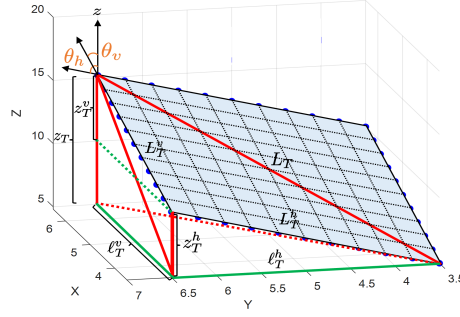


Fig. 8: TX Surface in Cartesian coordinates.

where  $\stackrel{(1)}{=}$  holds by noticing that  $z_T = z_T^h + z_T^v$ . Equaling both expressions of  $L_T^2$ , we get the following equation that should be satisfied if the surface (and element) is rectangle (or square)

$$(L_T^h \cos \theta_h)^2 + (L_T^v \cos \theta_v)^2 = (L_T^h \cos \theta_h + L_T^v \cos \theta_v)^2 \Rightarrow (L_T^h \cos \theta_h) (L_T^v \cos \theta_v) = 0.$$

It is obvious that  $\theta_h$  and  $\theta_v$  should be the angle that guarantees either  $\cos \theta_h$  or  $\cos \theta_v$  to be zero. Considering the practical placement of the surface, both angles are within the range of  $[0, 180^\circ]$ , such that we obtain  $\theta_h = 90^\circ$  or  $\theta_v = 90^\circ$ . We can similarly derive the results for RX as  $\vartheta_h = 90^\circ$  or  $\vartheta_v = 90^\circ$ , which completes the proof.

## APPENDIX B

### PROOF OF LEMMA 2

For any arbitrary  $\Delta \mathbf{t}_n = [\Delta x_n \ \Delta y_n \ \Delta z_n]^T$ , it can be represented by the combination of the horizontal unit vector  $\mathbf{t}_T^h = [\sin \theta_h \cos \phi_h \ \sin \theta_h \sin \phi_h \ \cos \theta_h]^T$  and the vertical unit vector  $\mathbf{t}_T^v = [\sin \theta_v \cos \phi_v \ \sin \theta_v \sin \phi_v \ \cos \theta_v]^T$  with weights, i.e.,  $\alpha$  and  $\beta$ , respectively. We thus have

$$\Delta \mathbf{t}_n = \alpha \mathbf{t}_T^h + \beta \mathbf{t}_T^v = \begin{bmatrix} \alpha \sin \theta_h \cos \phi_h + \beta \sin \theta_v \cos \phi_v \\ \alpha \sin \theta_h \sin \phi_h + \beta \sin \theta_v \sin \phi_v \\ \alpha \cos \theta_h + \beta \cos \theta_v \end{bmatrix}.$$

In order to derive  $\Delta z_n$ , represented by  $\Delta x_n$  and  $\Delta y_n$ , we need to first derive  $\alpha$  and  $\beta$ . To this aim, we multiply  $\Delta x_n$  with  $\sin \phi_v$ , and  $\Delta y_n$  with  $\cos \phi_v$ , respectively, yielding

$$\Delta x_n \sin \phi_v = \alpha \sin \theta_h \cos \phi_h \sin \phi_v + \beta \sin \theta_v \cos \phi_v \sin \phi_v,$$

$$\Delta y_n \cos \phi_v = \alpha \sin \theta_h \sin \phi_h \cos \phi_v + \beta \sin \theta_v \sin \phi_v \cos \phi_v.$$

Conducting a subtraction, we get

$$\Delta x_n \sin \phi_v - \Delta y_n \cos \phi_v = \alpha \sin \theta_h \sin (\phi_v - \phi_h), \Rightarrow \alpha = \frac{(\Delta x_n \sin \phi_v - \Delta y_n \cos \phi_v)}{\sin \theta_h \sin (\phi_v - \phi_h)}$$

when  $\sin \theta_h \neq 0$  and  $\sin (\phi_v - \phi_h) \neq 0$ . Similarly, multiplying  $\Delta x_n$  with  $\sin \phi_h$ , and  $\Delta y_n$  with  $\cos \phi_h$ , respectively, and then making a subtraction, we derive

$$\Delta x_n \sin \phi_h - \Delta y_n \cos \phi_h = \beta \sin \theta_v \sin (\phi_h - \phi_v), \Rightarrow \beta = \frac{(\Delta x_n \sin \phi_h - \Delta y_n \cos \phi_h)}{\sin \theta_v \sin (\phi_h - \phi_v)}$$

for  $\sin \theta_v \neq 0$  and  $\sin (\phi_h - \phi_v) \neq 0$ . With the availability of  $\alpha$  and  $\beta$ , we can obtain  $\Delta z_n$  as

$$\Delta z_n = \alpha \cos \theta_h + \beta \cos \theta_v = \frac{\cot \theta_v \sin \phi_n - \cot \theta_h \sin \phi_v}{\sin (\phi_h - \phi_v)} \Delta x_n + \frac{\cot \theta_v \cos \phi_h - \cot \theta_h \cos \phi_v}{\sin (\phi_h - \phi_v)} \Delta y_n.$$

Following a similar derivation process, for any arbitrary point  $\Delta \mathbf{r}_m = [\Delta x_m \ \Delta y_m \ \Delta z_m]^T \in s_R$ ,  $\Delta z_m$  can be represented via  $\{\Delta x_m, \Delta y_m\}$ , which completes the proof.

## APPENDIX C

### PROOF OF THEOREM 1

Based upon Lemma 2, we can proceed to derive  $I_T$  and  $I_R$ , respectively, where  $I_T$  is first derived as follows. By expanding the integral over the surface area by integrals over the horizontal length and the vertical length, we first obtain

$$I_T = \int_{s_T} e^{-ik_0 \frac{d_{mn}^T}{d_{mn}} \Delta \mathbf{t}_n} d\Delta \mathbf{t}_n = \int_{-\frac{l_T^v}{2}}^{\frac{l_T^v}{2}} \int_{-\frac{l_T^h}{2}}^{\frac{l_T^h}{2}} e^{-ik_0 \frac{\bar{x}_{mn} \Delta x_n + \bar{y}_{mn} \Delta y_n + \bar{z}_{mn} \Delta z_n}{d_{mn}}} d\Delta x_n d\Delta y_n$$

Inside, we define  $\bar{x}_{mn} \triangleq \bar{x}_m - \bar{x}_n$ ,  $\bar{y}_{mn} \triangleq \bar{y}_m - \bar{y}_n$ ,  $\bar{z}_{mn} \triangleq \bar{z}_m - \bar{z}_n$ ; Further replacing  $\Delta z_n$  with  $\Delta x_n$  and  $\Delta y_n$  via (15), and substituting it into  $I_T$ , we get

$$I_T = \int_{-\frac{l_T^h}{2}}^{\frac{l_T^h}{2}} e^{-ik_0 \frac{(\bar{x}_{mn} + \bar{z}_{mn} \frac{\sin \phi_h \cot \theta_v - \sin \phi_v \cot \theta_h}{\sin (\phi_h - \phi_v)}) \Delta x_n}{d_{mn}}} d\Delta x_n \int_{-\frac{l_T^v}{2}}^{\frac{l_T^v}{2}} e^{-ik_0 \frac{(\bar{y}_{mn} + \bar{z}_{mn} \frac{\cos \phi_h \cot \theta_v - \cos \phi_v \cot \theta_h}{\sin (\phi_h - \phi_v)}) \Delta y_n}{d_{mn}}} d\Delta y_n.$$

The integrals can be computed via the Euler's formula  $e^{ix} = \cos x + i \sin x$  and  $\text{sinc}(x) = \frac{\sin x}{x}$

$$I_T = l_T^h l_T^v \cdot \text{sinc} \left( \frac{\pi l_T^h}{\lambda} \cdot \frac{\bar{x}_{mn} + \bar{z}_{mn} \frac{\sin \phi_h \cot \theta_v - \sin \phi_v \cot \theta_h}{\sin (\phi_h - \phi_v)}}{\bar{d}_{mn}} \right) \text{sinc} \left( \frac{\pi l_T^v}{\lambda} \cdot \frac{\bar{y}_{mn} + \bar{z}_{mn} \frac{\cos \phi_h \cot \theta_v - \cos \phi_v \cot \theta_h}{\sin (\phi_h - \phi_v)}}{\bar{d}_{mn}} \right).$$

Employing (16) and performing a similar derivation process, we have  $I_R$  directly expressed as

$$\begin{aligned} I_R &= \int_{s_R} e^{ik_0 \frac{d_{mn}^T}{d_{mn}} \Delta \mathbf{r}_m} d\Delta \mathbf{r}_m \\ &= l_R^h l_R^v \cdot \text{sinc} \left( \frac{\pi l_R^h}{\lambda} \cdot \frac{\bar{x}_{mn} + \bar{z}_{mn} \frac{\sin \psi_h \cot \vartheta_v - \sin \psi_v \cot \vartheta_h}{\sin (\psi_h - \psi_v)}}{\bar{d}_{mn}} \right) \text{sinc} \left( \frac{\pi l_R^v}{\lambda} \cdot \frac{\bar{y}_{mn} + \bar{z}_{mn} \frac{\cos \psi_h \cot \vartheta_v - \cos \psi_v \cot \vartheta_h}{\sin (\psi_h - \psi_v)}}{\bar{d}_{mn}} \right). \end{aligned}$$

Substituting  $I_T$  and  $I_R$  into (21), we get the channel model (24), which completes the proof.

## APPENDIX D

## PROOF OF LEMMA 3

We first define an arbitrary point  $\mathbf{r} \in A$ . It is obvious to know that  $\mathbf{r}$  is within the region of a certain antenna element. Without loss of generality, we assume that  $\mathbf{r} = \mathbf{r}_k$  associates with the  $k$ -th antenna element, which can be represented by  $\mathbf{r}_k = \bar{\mathbf{r}}_k + \Delta\mathbf{r}_k$ , where  $\bar{\mathbf{r}}_k$  is the element center and  $\Delta\mathbf{r}_k$  belongs to area  $S$ . Then, the integral of two differentiable functions,  $\mathbf{f}(\mathbf{r})$  and  $\mathbf{g}(\mathbf{r})$ , over the surface area  $A$  can be reformulated as

$$\int_A \mathbf{f}^H(\mathbf{r})\mathbf{g}(\mathbf{r})d\mathbf{r} = \sum_{k=1}^K \int_S \mathbf{f}^H(\mathbf{r}_k)\mathbf{g}(\mathbf{r}_k)d\mathbf{r}_k = \sum_{k=1}^K \int_S \mathbf{f}^H(\bar{\mathbf{r}}_k + \Delta\mathbf{r}_k)\mathbf{g}(\bar{\mathbf{r}}_k + \Delta\mathbf{r}_k)d\Delta\mathbf{r}_k,$$

By further writing  $\mathbf{f}(\bar{\mathbf{r}}_k + \Delta\mathbf{r}_k)$  and  $\mathbf{g}(\bar{\mathbf{r}}_k + \Delta\mathbf{r}_k)$  via the Taylor series expansion, we have the following expressions and their approximations

$$\begin{aligned} \mathbf{f}(\bar{\mathbf{r}}_k + \Delta\mathbf{r}_k) &= \mathbf{f}(\bar{\mathbf{r}}_k) + \mathbf{J}_f(\bar{\mathbf{r}}_k) \Delta\mathbf{r}_k + o(\|\bar{\mathbf{r}}_k\|_2^2) \approx \mathbf{f}(\bar{\mathbf{r}}_k), \\ \mathbf{g}(\bar{\mathbf{r}}_k + \Delta\mathbf{r}_k) &= \mathbf{g}(\bar{\mathbf{r}}_k) + \mathbf{J}_g(\bar{\mathbf{r}}_k) \Delta\mathbf{r}_k + o(\|\bar{\mathbf{r}}_k\|_2^2) \approx \mathbf{g}(\bar{\mathbf{r}}_k), \end{aligned}$$

where  $\mathbf{J}_f(\mathbf{r})$  and  $\mathbf{J}_g(\mathbf{r})$  denote the Jacobian matrices of function  $\mathbf{f}(\mathbf{r})$  and  $\mathbf{g}(\mathbf{r})$ , respectively. The approximations hold due to the infinitesimal area of the antenna elements. As a consequence, we have the integral well approximated as

$$\int_A \mathbf{f}^H(\mathbf{r})\mathbf{g}(\mathbf{r})d\mathbf{r} \approx \sum_{k=1}^K \int_S \mathbf{f}^H(\bar{\mathbf{r}}_k)\mathbf{g}(\bar{\mathbf{r}}_k)d\Delta\mathbf{r}_k = \sum_{k=1}^K \mathbf{f}^H(\bar{\mathbf{r}}_k)\mathbf{g}(\bar{\mathbf{r}}_k) \int_S d\Delta\mathbf{r}_k \approx S \sum_{k=1}^K \mathbf{f}^H(\bar{\mathbf{r}}_k)\mathbf{g}(\bar{\mathbf{r}}_k),$$

which completes the proof.

## APPENDIX E

## PROOF OF THEOREM 2

To transform the unknown  $\gamma_{pp}$  to some known replacements, we resort to the concave property of the  $\log_2(\cdot)$  function. As such, using the Jensen's inequality, we get the capacity upper bounded

$$\begin{aligned} C &= \log_2 \left( \prod_{p=1}^P (1 + \mu \cdot \text{SNR} \cdot \gamma_{pp}^2) \right) \stackrel{(1)}{\leq} P \cdot \log_2 \left( \frac{1}{P} \sum_{p=1}^P (1 + \mu \cdot \text{SNR} \cdot \gamma_{pp}^2) \right) \\ &\stackrel{(2)}{=} P \cdot \log_2 \left( 1 + \frac{\mu \text{SNR}}{P} \int_{A_R} \int_{A_T} \|\mathbf{G}(\mathbf{r}_m, \mathbf{t}_n)\|^2 d\mathbf{t}_n d\mathbf{r}_m \right), \end{aligned}$$

where  $\stackrel{(1)}{\leq}$  holds by using the inequality between the arithmetic mean and the geometric mean, i.e.,

$$\prod_{p=1}^P x_p \leq \left( \frac{1}{P} \sum_{p=1}^P x_p \right)^P \text{ for } x_p \geq 0; \stackrel{(2)}{=} \text{ is obtained using } \sum_{p=1}^P \gamma_{pp}^2 = \int_{A_R} \int_{A_T} \|\mathbf{G}(\mathbf{r}_m, \mathbf{t}_n)\|^2 d\mathbf{t}_n d\mathbf{r}_m$$

derived in [25, Appendix A] that can be dated back to [26, Appendix B]. To present a more explicit result of this upper bound, we apply the tensor Green's function (17) and obtain

$$\begin{aligned}
C &\leq P \cdot \log_2 \left( 1 + \frac{\mu \cdot \text{SNR}}{P} \cdot \int_{A_R} \int_{A_T} \text{trace} [\mathbf{G}^H(\mathbf{r}_m, \mathbf{t}_n) \mathbf{G}(\mathbf{r}_m, \mathbf{t}_n)] d\mathbf{t}_n d\mathbf{r}_m \right) \\
&= P \cdot \log_2 \left( 1 + \frac{\mu \cdot \text{SNR}}{P} \cdot \sum_{m=1}^M \sum_{n=1}^N \int_{s_R} \int_{s_T} \text{trace} (\mathbf{G}^H(\mathbf{r}_m, \mathbf{t}_n) \mathbf{G}(\mathbf{r}_m, \mathbf{t}_n)) d\mathbf{t}_n d\mathbf{r}_m \right) \\
&\approx P \cdot \log_2 \left( 1 + \frac{\mu \cdot \text{SNR}}{P} \cdot s_{RST} \cdot \sum_{m=1}^M \sum_{n=1}^N \text{trace} (\mathbf{G}^H(\bar{\mathbf{r}}_m, \bar{\mathbf{t}}_n) \mathbf{G}(\bar{\mathbf{r}}_m, \bar{\mathbf{t}}_n)) \right) \\
&= P \cdot \log_2 \left( 1 + \frac{\mu \cdot \text{SNR}}{P} \cdot s_{RST} \cdot \sum_{m=1}^M \sum_{n=1}^N \left( \frac{\varepsilon_1}{\bar{d}_{mn}^2} + \frac{\varepsilon_2}{\bar{d}_{mn}^4} + \frac{\varepsilon_3}{\bar{d}_{mn}^6} \right) \right),
\end{aligned}$$

where the approximation holds for infinitesimal antenna elements, and is obtained based on Lemma 3; the coefficients are given by (48a) (48b) (48c), which completes this proof.

## REFERENCES

- [1] T. Gong, L. Wei, Z. Yang, M. Debbah, and C. Yuen, "A generalized electromagnetic-domain channel modeling for LOS holographic MIMO with arbitrary surface placements," *arXiv preprint arXiv:2303.08482*, 2023.
- [2] W. Saad, M. Bennis, and M. Z. Chen, "A vision of 6G wireless systems: Applications, trends, technologies, and open research problems," *IEEE Netw.*, vol. 34, no. 3, pp. 134–142, Jun. 2020.
- [3] M. Xiao, S. Mumtaz, Y. Huang, L. Dai, Y. Li, M. Matthaiou, G. K. Karagiannidis, E. Björnson, K. Yang, C.-L. I, and A. Ghosh, "Millimeter wave communications for future mobile networks," *IEEE J. Sel. Areas Commun.*, vol. 35, no. 9, pp. 1909–1935, 2017.
- [4] A. F. Molisch, V. V. Ratnam, S. Han, Z. Li, S. L. H. Nguyen, L. Li, and K. Haneda, "Hybrid beamforming for massive MIMO: A survey," *IEEE Commun. Mag.*, vol. 55, no. 9, pp. 134–141, 2017.
- [5] T. Gong, N. Shlezinger, S. S. Ioushua, M. Namer, Z. Yang, and Y. C. Eldar, "RF chain reduction for MIMO systems: A hardware prototype," *IEEE Syst. J.*, vol. 14, no. 4, pp. 5296–5307, Dec. 2020.
- [6] T. Gong, I. Vinieratou, R. Ji, C. Huang, G. C. Alexandropoulos, L. Wei, Z. Zhang, M. Debbah, H. V. Poor, and C. Yuen, "Holographic MIMO communications: Theoretical foundations, enabling technologies, and future directions," *arXiv preprint arXiv:2212.01257*, 2022.
- [7] C. Huang, S. Hu, G. C. Alexandropoulos, A. Zappone, C. Yuen, R. Zhang, M. Di Renzo, and M. Debbah, "Holographic MIMO surfaces for 6G wireless networks: Opportunities, challenges, and trends," *IEEE Wireless Commun.*, vol. 27, no. 5, pp. 118–125, Oct. 2020.
- [8] D. Dardari and N. Decarli, "Holographic communication using intelligent surfaces," *IEEE Commun. Mag.*, vol. 59, no. 6, pp. 35–41, Jun. 2021.
- [9] T. L. Marzetta, "Super-directive antenna arrays: Fundamentals and new perspectives," in *Proc. 2019 53th Asilomar Conf. Signals, Sys., Comp.*, Nov. 2019, pp. 1–4.
- [10] D. Tse and P. Viswanath, *Fundamentals of wireless communication*. Cambridge university press, 2005.
- [11] E. Björnson, J. Hoydis, and L. Sanguinetti, "Massive MIMO has unlimited capacity," *IEEE Trans. Wireless Commun.*, vol. 17, no. 1, pp. 574–590, Jan. 2018.

- [12] R. W. Heath, N. González-Prelcic, S. Rangan, W. Roh, and A. M. Sayeed, “An overview of signal processing techniques for millimeter wave MIMO systems,” *IEEE J. Sel. Topics Signal Process.*, vol. 10, no. 3, pp. 436–453, Apr. 2016.
- [13] Y. Cheng, W. Peng, C. Huang, G. C. Alexandropoulos, C. Yuen, and M. Debbah, “RIS-aided wireless communications: Extra degrees of freedom via rotation and location optimization,” *IEEE Trans. Wireless Commun.*, vol. 21, no. 8, pp. 6656–6671, 2022.
- [14] A. Pizzo, T. L. Marzetta, and L. Sanguinetti, “Spatially-stationary model for holographic MIMO small-scale fading,” *IEEE J. Sel. Areas Commun.*, vol. 38, no. 9, pp. 1964–1979, Sep. 2020.
- [15] A. Pizzo, L. Sanguinetti, and T. L. Marzetta, “Fourier plane-wave series expansion for holographic MIMO communications,” *IEEE Trans. Wireless Commun.*, pp. 1–1, Sep. 2022.
- [16] L. Wei, C. Huang, G. Alexandropoulos, W. E. I. Sha, Z. Zhang, M. Debbah, and C. Yuen, “Multi-user holographic MIMO surfaces: Channel modeling and spectral efficiency analysis,” *IEEE J. Sel. Topics Signal Process.*, pp. 1–1, Aug. 2022.
- [17] H. Zhang, N. Shlezinger, F. Guidi, D. Dardari, M. F. Imani, and Y. C. Eldar, “Beam focusing for near-field multi-user MIMO communications,” *IEEE Trans. Wireless Commun.*, pp. 1–1, Sep. 2022.
- [18] M. Cui and L. Dai, “Channel estimation for extremely large-scale MIMO: Far-field or near-field?” *IEEE Trans. Commun.*, vol. 70, no. 4, pp. 2663–2677, Apr. 2022.
- [19] L. Wei, C. Huang, G. C. Alexandropoulos, Z. Yang, J. Yang, W. E. I. Sha, Z. Zhang, M. Debbah, and C. Yuen, “Tri-polarized holographic MIMO surface in near-field: Channel modeling and precoding design,” *arXiv preprint arXiv:2211.03479*, 2022.
- [20] S. Hu, F. Rusek, and O. Edfors, “Beyond massive MIMO: The potential of data transmission with large intelligent surfaces,” *IEEE Trans. Signal Process.*, vol. 66, no. 10, pp. 2746–2758, May 2018.
- [21] A. de Jesus Torres, L. Sanguinetti, and E. Björnson, “Near- and far-field communications with large intelligent surfaces,” in *Proc. 2020 54th Asilomar Conf. Signals, Sys., Comp.*, Nov. 2020, pp. 564–568.
- [22] H. Lu and Y. Zeng, “Communicating with extremely large-scale array/surface: Unified modeling and performance analysis,” *IEEE Trans. Wireless Commun.*, vol. 21, no. 6, pp. 4039–4053, Jun. 2022.
- [23] A. Poon, R. Brodersen, and D. Tse, “Degrees of freedom in multiple-antenna channels: a signal space approach,” *IEEE Trans. Inf. Theory*, vol. 51, no. 2, pp. 523–536, Feb. 2005.
- [24] P. Wang, M. Nasiri Khormuji, and B. M. Popovic, “Performances of LoS holographic radio systems,” in *Proc. 2022 IEEE Int. Conf. Commun. (ICC)*, May 2022, pp. 3299–3304.
- [25] D. Dardari, “Communicating with large intelligent surfaces: Fundamental limits and models,” *IEEE J. Sel. Areas Commun.*, vol. 38, no. 11, pp. 2526–2537, Nov. 2020.
- [26] R. Piestun and D. A. Miller, “Electromagnetic degrees of freedom of an optical system,” *J. Opt. Soc. Am.*, vol. 17, no. 5, pp. 892–902, 2000.
- [27] D. A. B. Miller, “Communicating with waves between volumes: evaluating orthogonal spatial channels and limits on coupling strengths,” *Appl. Opt.*, vol. 39, no. 11, pp. 1681–1699, Apr 2000.
- [28] W. C. Chew, *Waves and fields in inhomogenous media*. John Wiley & Sons, 1999.
- [29] H. F. Arnoldus, “Representation of the near-field, middle-field, and far-field electromagnetic Green’s functions in reciprocal space,” *JOSA B*, vol. 18, no. 4, pp. 547–555, 2001.
- [30] A. Goldsmith, S. Jafar, N. Jindal, and S. Vishwanath, “Capacity limits of MIMO channels,” *IEEE J. Sel. Areas Commun.*, vol. 21, no. 5, pp. 684–702, 2003.
- [31] L. Sanguinetti, A. A. D’Amico, and M. Debbah, “Wavenumber-division multiplexing in line-of-sight holographic MIMO communications,” *IEEE Trans. Wireless Commun.*, 2022.
- [32] Z. Zhang and L. Dai, “Pattern-division multiplexing for multi-user continuous-aperture MIMO,” *arXiv preprint arXiv:2111.08630v2*, 2022.